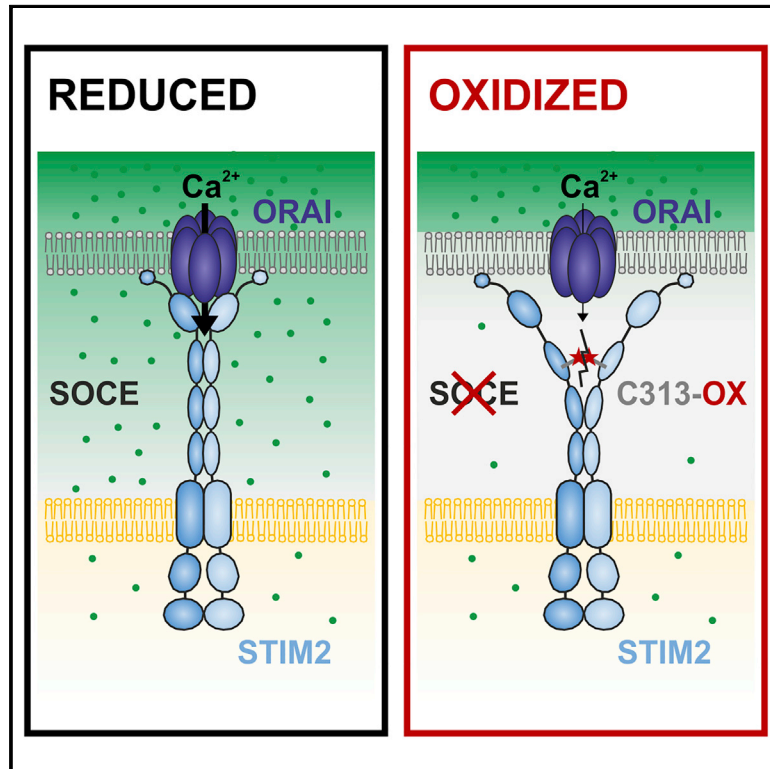# Oxidative Stress-Induced STIM2 Cysteine Modifications Suppress Store-Operated Calcium Entry

Graphical Abstract

Authors

Christine Silvia Gibhardt,
Sabrina Cappello, Rajesh Bhardwaj, ...,
Matthias Albrecht Hediger,
Rainer Schindl, Ivan Bogeski

Correspondence

rainer.schindl@medunigraz.at (R.S.),
ivan.bogeski@med.uni-goettingen.de
(I.B.)

In Brief

The ER-residing STIM2 protein gates ORAI Ca^{2+} channels at the plasma membrane. However, the functional relevance of STIM2 is not fully understood. Gibhardt et al. reveal a regulatory mechanism in which oxidation of C313 controls STIM2 function. Oxidative stress-induced C313 sulfonylation hinders STIM2 oligomerization, causing inhibition of store-operated Ca^{2+} entry.

Highlights

- Compared with STIM1, STIM2 has 10 additional cytosolic cysteines

- STIM2 oxidation inhibits store-operated Ca^{2+} entry

- Redox proteomics identifies C313 as the redox sensor of STIM2

- Oxidation of C313 prevents STIM2-STIM2 oligomerization

CellPress

Cell Reports

Article

Oxidative Stress-Induced STIM2 Cysteine Modifications Suppress Store-Operated Calcium Entry

Christine Silvia Gibhardt,[1] Sabrina Cappello,[1] Rajesh Bhardwaj,[2] Romana Schober,[3,10] Sonja Agnes Kirsch,[4] Zuriñe Bonilla del Rio,[1] Stefan Gahbauer,[4,11] Anna Bochicchio,[4] Magdalena Sumanska,[1] Christian Ickes,[1] Ioana Stejerean-Todoran,[1] Miso Mitkovski,[5] Dalia Alansary,[6] Xin Zhang,[1] Aram Revazian,[1] Marc Fahrner,[3] Victoria Lunz,[3] Irene Frischauf,[3] Ting Luo,[7] Daria Ezerina,[7] Joris Messens,[7] Vsevolod Vadimovich Belousov,[1,8,9] Markus Hoth,[6] Rainer Arnold Böckmann,[4] Matthias Albrecht Hediger,[2] Rainer Schindl,[10,*] and Ivan Bogeski[1,12,*]

[1]Molecular Physiology, Institute of Cardiovascular Physiology, University Medical Center, Georg-August-University, Göttingen, Germany
[2]Department of Nephrology and Hypertension, Inselspital, University of Bern, Bern, Switzerland
[3]Institute of Biophysics, JKU Life Science Center, Johannes Kepler University Linz, Linz, Austria
[4]Computational Biology, Department of Biology, Friedrich-Alexander University of Erlangen-Nürnberg, Germany
[5]Light Microscopy Facility, Max Planck Institute of Experimental Medicine, Göttingen, Germany
[6]Biophysics, Center for Integrative Physiology and Molecular Medicine, Saarland University, Homburg, Germany
[7]VIB-VUB Center for Structural Biology, Brussels Center for Redox Biology, Structural Biology Brussels, Vrije Universiteit Brussel, Brussels, Belgium
[8]Pirogov Russian National Research Medical University, Moscow, Russia
[9]Federal Center of Brain Research and Neurotechnologies of the Federal Medical Biological Agency, Moscow, Russia
[10]Gottfried Schatz Research Center, Medical University of Graz, Graz, Austria
[11]Present address: Department of Pharmaceutical Chemistry, University of California, San Francisco, San Francisco, CA, USA
[12]Lead Contact
*Correspondence: rainer.schindl@medunigraz.at (R.S.), ivan.bogeski@med.uni-goettingen.de (I.B.)
https://doi.org/10.1016/j.celrep.2020.108292

SUMMARY

Store-operated calcium entry (SOCE) through STIM-gated ORAI channels governs vital cellular functions. In this context, SOCE controls cellular redox signaling and is itself regulated by redox modifications. However, the molecular mechanisms underlying this calcium-redox interplay and the functional outcomes are not fully understood. Here, we examine the role of STIM2 in SOCE redox regulation. Redox proteomics identify cysteine 313 as the main redox sensor of STIM2 *in vitro* and *in vivo*. Oxidative stress suppresses SOCE and calcium currents in cells overexpressing STIM2 and ORAI1, an effect that is abolished by mutation of cysteine 313. FLIM and FRET microscopy, together with MD simulations, indicate that oxidative modifications of cysteine 313 alter STIM2 activation dynamics and thereby hinder STIM2-mediated gating of ORAI1. In summary, this study establishes STIM2-controlled redox regulation of SOCE as a mechanism that affects several calcium-regulated physiological processes, as well as stress-induced pathologies.

INTRODUCTION

SOCE and CRAC Channels

Store-operated calcium entry (SOCE) through stromal interaction molecule (STIM)-gated ORAI channels is a major calcium (Ca^{2+}) entry route in cells. SOCE is responsible for controlling cellular functions such as proliferation, differentiation, gene regulation, and secretion (Parekh and Putney, 2005; Prakriya and Lewis, 2015). SOCE is also involved in several pathological conditions; cancer, immune deficiency, tubular aggregate myopathy, and other severe diseases are known to be determined by mutations or perturbed expression levels of the key SOCE-regulating proteins (Ambudkar, 2018; Fahrner et al., 2018; Feske et al., 2006; Picard et al., 2009; Prevarskaya et al.,

2011; Stanisz et al., 2014, 2016). SOCE is typically initiated by the engagement of surface receptors that cause cytosolic production of inositol trisphosphate (IP_3) and activation of endoplasmic reticulum (ER)-based IP_3 receptors (IP_3Rs), which release Ca^{2+} from the ER and lead to activation of a Ca^{2+} release-activated Ca^{2+} current (I_{CRAC}) through plasma membrane Ca^{2+} release-activated Ca^{2+} (CRAC) channels (Hoth and Penner, 1992). Five proteins represent the main molecular determinants of the CRAC channels: ORAI1 and its homologs ORAI2 and ORAI3 are the channel-forming subunits within the plasma membrane, whereas STIM1 and STIM2 are responsible for sensing the luminal ER Ca^{2+} levels and gating of ORAI channels (Carrasco and Meyer, 2011; Hogan et al., 2010; Hoth and Niemeyer, 2013; Prakriya and Lewis, 2015; Soboloff et al., 2012).
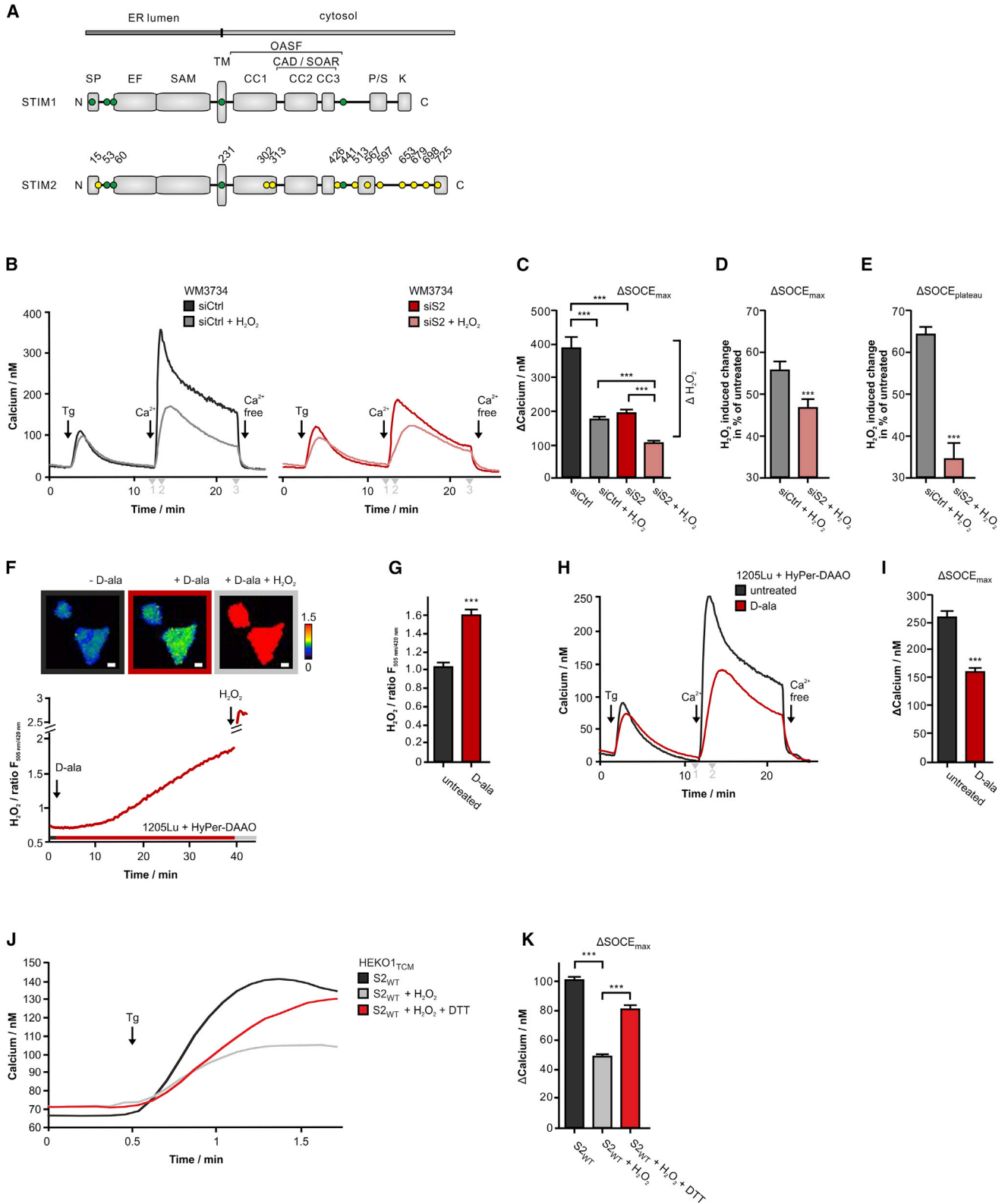
STIM Structure and Function

STIM1 and STIM2 are localized in the ER membrane and sense luminal ER Ca^{2+} via an N-terminally located, classical EF-hand structure (Stathopulos et al., 2008) (Figure 1A). In the cytosolic part, both STIM1 and STIM2 have three coiled-coil domains (CC1, CC2, and CC3) and a lysine (Lys)-rich domain that binds to the plasma membrane phosphatidylinositol 4,5-bisphosphate ($PI(4,5)P_2$) upon activation (Liou et al., 2007). The second and third coiled-coil domains form the so-called CAD (CRAC activating domain) or SOAR (STIM-ORAI activating region), which directly interacts with and gates the pore-forming ORAI channels (Park et al., 2009; Yuan et al., 2009). In the resting state of STIM1 and STIM2, their CAD/SOAR domain is shielded by an interaction with CC1 (Korzeniowski et al., 2010; Muik et al., 2011; Subedi et al., 2018). Upon STIM1 activation, CC1 detaches from the CAD/SOAR structure (this two-domain construct is named OASF, for ORAI activating small fragment) to allow ORAI binding, as well as interaction with the plasma membrane. Hence, CC1 plays an important role in maintaining a closed and compressed configuration to finally restrict and control interaction with ORAI channels (Fahrner et al., 2014, 2018; Subedi et al., 2018). Although STIM1 and STIM2 have several highly conserved domains and both activate the ORAI channels, they manifest physiologically different functions in many cellular systems. For example, STIM2 responds to small changes in ER Ca^{2+} concentrations, whereas STIM1 requires substantial store depletion (Brandman et al., 2007; Zheng et al., 2011). STIM1 is also more efficient in generating large ORAI-mediated Ca^{2+} signals in comparison to STIM2 (Wang et al., 2014). STIM2 has recently been reported to facilitate the coupling of ORAI1 function with nuclear factor of activated T-cells 1 (NFAT1) activation (Son et al., 2020). Moreover, STIM2 has been identified as an important regulator of cell physiology and pathology, particularly in immune cells, neuronal cells, and other cells originating from the neural crest, such as melanocytes and melanoma (Berna-Erro et al., 2009, 2017; Cheng et al., 2012; Clemens et al., 2017; Diercks et al., 2018; Shaw et al., 2014; Stanisz et al., 2012, 2014; Sun et al., 2014; Yoshikawa et al., 2019).

Redox Regulation of Ca^{2+} Channels

Protein function can be regulated by redox modifications of reactive cysteines, but methionine residues and other amino acids can also be oxidized under more extreme conditions. Redox modifications are typically induced through chemically (reactive oxygen species [ROS], H_2S) or enzymatically driven electron transfer, which alters the protein redox status and thereby its function (Rhee, 1999; Sies et al., 2017; Winterbourn and Hampton, 2008). We and others have shown that CRAC channels, transient receptor potential (TRP) channels, IP_3Rs, and voltage-gated Ca^{2+} channels can be controlled via redox modifications and can thus influence several physiological and pathophysiological conditions (for details, see Bhardwaj et al., 2016; Bogeski et al., 2011; Bogeski and Niemeyer, 2014; Nunes and Demaurex, 2014; Trebak et al., 2010). Compared with its homolog STIM1, STIM2 has ten additional cysteine residues in the cytosolic domain whose functional importance was not understood. Here, we explore the role of these STIM2-specific cysteines in the context of SOCE redox regulation.

RESULTS

Oxidative Stress Inhibits STIM2-Controlled SOCE

The schematic comparison of human STIM1 and STIM2 primary structures (Figure 1A) highlights the ten additional cytosolic cysteines (yellow circles) in STIM2 that suggest increased redox sensitivity of STIM2 over STIM1. In melanoma cells, STIM2 is the predominant STIM isoform and, together with ORAI1, controls their growth and invasion (Hooper et al., 2015; Stanisz et al., 2014). Therefore, we used melanoma cells to test whether STIM2 redox regulation affects SOCE. As seen in Figures 1B and 1C, silencing of STIM2 reduced SOCE in melanoma cells (black versus red), as previously reported (Stanisz et al., 2014). In addition, H_2O_2 treatment suppressed SOCE in both STIM2-silenced and STIM2-non-silenced cells (black versus gray and red versus light red). To extract the contribution of STIM2 redox regulation in this experimental setup (melanoma cells express ORAI1, which is also inhibited by H_2O_2), we normalized the H_2O_2-treated cells against their respective controls (black or red) and calculated the percentage of inhibition following H_2O_2 treatment. The quantifications depicted in Figure 1D (max) and Figure 1E (plateau) indicated that silencing of STIM2 significantly reduces the redox sensitivity of SOCE in melanoma cells. To evaluate whether this is a cell-line-specific effect, we performed the same measurements in a second melanoma cell line (1205Lu) and in primary human $CD4^+$ T cells. As depicted in Figures S1A–S1G, we could observe a significant

---

Figure 1. STIM2 Oxidation Reversibly Inhibits SOCE

(A) Schematic representation of the STIM1 and STIM2 primary structure. Cysteine residues are highlighted as dots (cysteines in STIM1 and STIM2, green; additional cysteines in STIM2, yellow). The long signal peptide (87 aa) of STIM2 is excluded from the current numbering.

(B–E) Ca^{2+} imaging of STIM2 small interfering RNA (siRNA)-treated WM3734 melanoma cells. (B) Calibrated Ca^{2+} traces with or without H_2O_2 pre-treatment (1 mM, 10–15 min). (C) Quantification of $\Delta SOCE_{max}$ ((2)-(1)). H_2O_2-induced inhibition of $\Delta SOCE_{max}$ (D) and $\Delta SOCE_{plateau}$ ((3)-(1)) (E) normalized to the untreated sample. Data are presented as mean ± SEM (n values: siCtrl = 166, siCtrl+H_2O_2 = 210, siS2 = 111, siS2+H_2O_2 = 184).

(F) HyPer-DAAO imaging in 1205Lu melanoma cells treated with 4 mM D-alanine (D-ala) and 1 mM H_2O_2, as indicated (n = 82, scale bars: 10 μm).

(G) H_2O_2 concentration following 60 min of D-ala (4 mM) treatment (n values: untreated = 63, D-ala = 104).

(H and I) Ca^{2+} imaging in 1205Lu melanoma cells. (H) Calibrated Ca^{2+} traces of cells with or without D-ala pre-treatment (4 mM, 60 min). (I) Corresponding quantification of $\Delta SOCE_{max}$ ((2)-(1)). Data are presented as mean ± SEM (n values: untreated = 82, D-ala = 145).

(J) Ca^{2+} imaging of HEKO1$_{TCM}$+S2$_{WT}$ cells with or without H_2O_2 (1 mM, 15 min) and DTT (2 mM, 15 min).

(K) Corresponding quantification of $\Delta SOCE_{max}$ (max-basal). Data are presented as mean ± SEM (n values: S2$_{WT}$ = 939, S2$_{WT}$+H_2O_2 = 620, S2$_{WT}$+H_2O_2+DTT = 675).

Statistical significance was addressed using unpaired, two-tailed Student's t test, ***p < 0.005. See also Figure S1.

contribution of STIM2 to SOCE redox regulation in both additional cell lines.

Treatment of cells with a bolus of H_2O_2 resembles a phagocyte oxidative burst to a certain degree and, with proper controls, can be used in answering physiological questions. Nevertheless, it was important to obtain greater insight into the molecular mechanisms of STIM2 redox regulation and better understand the physiological relevance. We thus overexpressed the yeast di-amino acid oxidase (DAAO, an enzyme that generates H_2O_2 in presence of D-amino acids) fused with the H_2O_2 biosensor Hy-Per in melanoma cells. This H_2O_2-inducer-sensor construct provided us the possibility to simultaneously generate and monitor intracellular H_2O_2 levels (for details, see Matlashov et al., 2014). Figures 1F and 1G show that addition of D-alanine causes a significant and gradual increase in cytosolic H_2O_2, thus mimicking physiological H_2O_2 production by enzymes such as the NADPH oxidases. Moreover, Ca^{2+} measurements in these DAAO-overexpressing melanoma cells indicated significant SOCE inhibition of around 35% following treatment with D-alanine (Figures 1H and 1I). Hence, we could conclude that both intracellular and extracellular oxidants can inhibit STIM2-controlled SOCE.

ORAI1, which is the predominant ORAI isoform in most cells, is inhibited by oxidation of a critical cysteine (C195) located in the extracellular space (Ben-Kasus Nissim et al., 2017; Bogeski et al., 2010). Hence, to precisely quantify the oxidation-induced effects of STIM2 on SOCE, it was essential to render ORAI1 redox insensitive. For this purpose, we developed an inducible HEK293 cell line overexpressing ORAI1 with no cysteines (HEKO1$_{TCM}$; triple-cysteine mutant [TCM], C195S + C143S + C126S). As seen in Figure S1H, stimulation with doxycycline induced a robust increase in ORAI1$_{TCM}$ expression after 12 h. Moreover, the cells exhibited typical Ca^{2+} transients following thapsigargin (Tg)-induced store depletion and concomitant Ca^{2+} entry following addition of 0.5 mM Ca^{2+} to the bath solution (Figures S1I and S1J). By using these cells, it was possible to evaluate the functional significance of STIM2 redox regulation on SOCE. As depicted in Figures 1J and 1K, HEKO1$_{TCM}$ cells were first exposed to H_2O_2 to induce cysteine oxidation and were subsequently treated with Tg to activate SOCE. The quantification of these traces showed that H_2O_2 treatment of cells overexpressing ORAI1$_{TCM}$ and STIM2$_{WT}$ (gray) caused inhibition of SOCE by more than 50% when compared with the untreated control (black). Moreover, we found that additional treatment with the thiol-reducing agent DTT (dithiothreitol, red) significantly reversed the H_2O_2-induced SOCE inhibition. In summary, these findings indicated that thiol modifications may play a central role in the STIM2-controlled redox regulation of SOCE.

Identification of STIM2 Reactive Cysteines

To address the role of thiol oxidative modifications and the additional cytosolic cysteines in STIM2 redox sensitivity, we initially used a MTSEA-biotin assay to quantify the total content of reactive cysteines (Figure 2A). Hydrogen peroxide treatment of HEK293 cells transiently overexpressing STIM2$_{WT}$ inhibited the MTSEA-biotin-bound STIM2$_{WT}$ fraction by around 2-fold when compared with the cells subsequently treated with DTT (Figures 2B and 2C). This approach indicated that at least some cysteines

in STIM2 are redox regulated following H_2O_2 treatment. To determine the identity of the reactive cysteines in STIM2, we next performed redox proteomic analysis (OxICAT) based on mass spectrometry (MS, specifically LC-MS/MS). HEK293 cells stably overexpressing STIM2$_{WT}$ (HEKS2$_{WT}$) were treated with H_2O_2 (oxidized state) or DTT (reduced state) and incubated sequentially with a light-isotope-labeled (^{12}C) and a heavy-isotope-labeled (^{13}C) isotope-coded affinity tag (ICAT), a chemical tool used for determining thiol oxidative modifications (Figure 2D) (Leichert et al., 2008; Lindemann and Leichert, 2012). This approach includes all cellular thiols and will identify the peptides with the highest abundance. Furthermore, only cysteines whose redox states were altered between the reducing and the oxidizing conditions are considered for further analysis. The quantification of the MS-based redox proteomics identified several peptides. Twenty peptides with the highest redox regulation are listed in Table S1. Among these, we identified three STIM2 peptides that displayed a significantly different abundance in the light and heavy ICAT-labeled fractions. Further analysis showed that the cysteine at position 302 (C302) and the cysteine at position 313 (C313) are modified by thiol oxidation (Figure 2E). Cross-species alignment (Figure 2F) indicated that C313 is more conserved than C302, suggesting that C313 might have a more prominent regulatory role.

Mimicking oxidative stress by treating cells with external H_2O_2 is a handy tool that is regularly used in detecting thiol oxidation, particularly when performing redox proteomics. Nevertheless, it was essential to explore whether STIM2 cysteine oxidation is regulated *in vivo*, under fully physiological conditions. To answer this question, we performed bioinformatic analyses of a public database provided by a recently published study that used redox proteomics to evaluate global cysteine oxidation in different tissues of young and aged mice (Xiao et al., 2020). As seen in Figure 2G, STIM2 C313 was oxidized in 9 of 20 conditions (from 10 tissues). This analysis indicated that STIM2 C313 is the major sensor of STIM2, given that the oxidation rate (percentage of occupancy) and the number of tissues in which its oxidation was detected were significantly higher compared with other STIM2 cysteine residues (Xiao et al., 2020). Interestingly, oxidation of C302 was not detected with this analysis.

Altogether, using different screening approaches, we identified C313 and possibly C302 as redox sensors of STIM2. Moreover, *in vivo* study confirmed that C313 can be oxidized under physiological conditions and without the addition of external oxidants.

STIM2 C313 Modulates SOCE Redox Sensitivity

To determine the functional importance of C302 and C313 in STIM2, we mutated each of them into valine or alanine residues. These STIM2 cysteine mutants were transiently overexpressed in HEKO1$_{TCM}$. The Ca^{2+} imaging experiments depicted in Figures S2A–S2D, indicated that the C302 and C313 mutants are functional and do not affect SOCE significantly under resting (not oxidized) environmental conditions. As demonstrated in Figure 1, H_2O_2 treatment inhibited SOCE in HEKO1$_{TCM}$ cells overexpressing STIM2$_{WT}$. To evaluate the contribution of STIM2's C302 and C313, we measured SOCE in HEKO1$_{TCM}$ cells overexpressing STIM2$_{WT}$, STIM2$_{C302V}$, or STIM2$_{C313V}$. Figures 3A and 3B
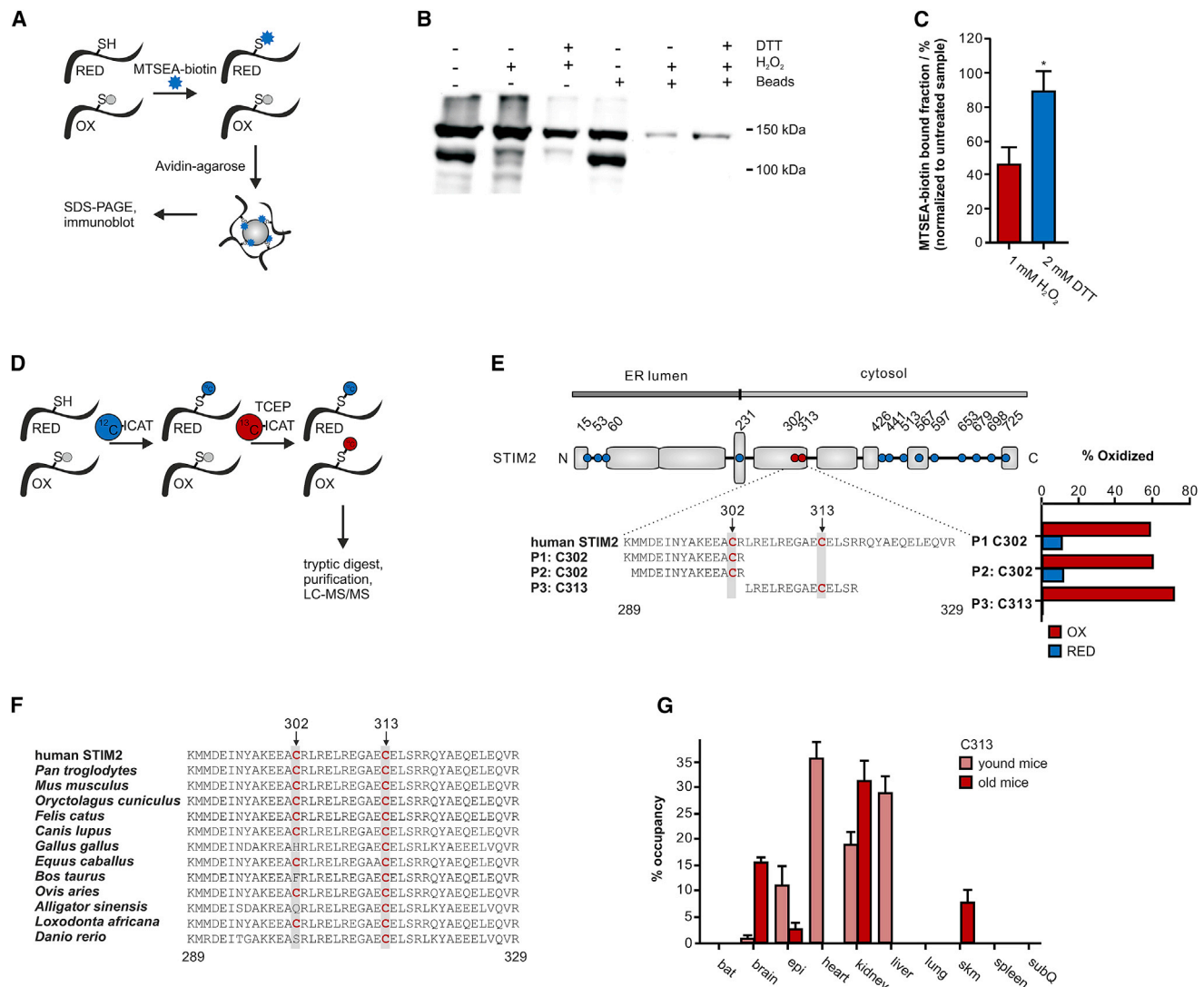
Figure 2. C302 and C313 in STIM2 Are Modified under Oxidative Stress

(A) Schematic representation of the MTSEA-biotin assay.

(B) Representative STIM2 immunoblot from untreated, H_2O_2-treated, and H_2O_2+DTT-treated cells.

(C) Quantification of MTSEA-bound fractions of S2$_{WT}$ under oxidizing conditions (1 mM H_2O_2) and reducing conditions (2 mM DTT) normalized to the untreated sample. Data are presented as mean ± SEM (n = 4).

(D) Schematic representation of the OxICAT redox proteomic method.

(E) Identified peptides by OxICAT redox proteomics in the CC1 domain of STIM2, indicating the percentage of oxidation of C302 and C313 in HEKS2$_{WT}$ cells under oxidizing (OX) conditions (1 mM H_2O_2) and reducing (RED) conditions (2 mM DTT).

(F) Sequence alignment of the CC1 domain (residues 289–329 of human STIM2), highlighting C302 and C313.

(G) Oximouse dataset (Xiao et al., 2020); quantification of STIM2 C313 oxidation as the percentage of occupancy from 16-week-old (young) and 80-week-old (old) male C57BL/6J mice. Data are presented as mean ± SEM.

BAT, brown adipose tissue; epi, epididymal fat; subQ, subcutaneous fat; SKM, skeletal muscle. Statistical significance was addressed using unpaired, two-tailed Student's t test, *p < 0.05. See also Table S1.

demonstrate that the H_2O_2-induced SOCE inhibition was reduced in cells overexpressing the STIM2$_{C302V}$ mutant (green) and almost fully abolished in cells overexpressing the STIM2$_{C313V}$ mutant (blue). These measurements were also performed with HEKO1$_{TCM}$ cells overexpressing STIM2 C302 and C313 alanine mutants. The results presented in Figures S2E and S2F depict similar behavior when compared with the valine

mutants. Moreover, Ca^{2+} measurements in HEK cells lacking STIM1 and STIM2 (HEKS1$_{KO}$S2$_{KO}$) and transiently overexpressing ORAI1$_{TCM}$ and STIM2$_{WT}$ or STIM2$_{C313V}$ indicated that endogenous STIM levels do not significantly affect SOCE redox regulation in an overexpressing system such as HEKO1$_{TCM}$+S2$_{WT/C313V}$ (Figures S2G and S2H). Next, we sought to test whether and how other stimuli that induce cellular
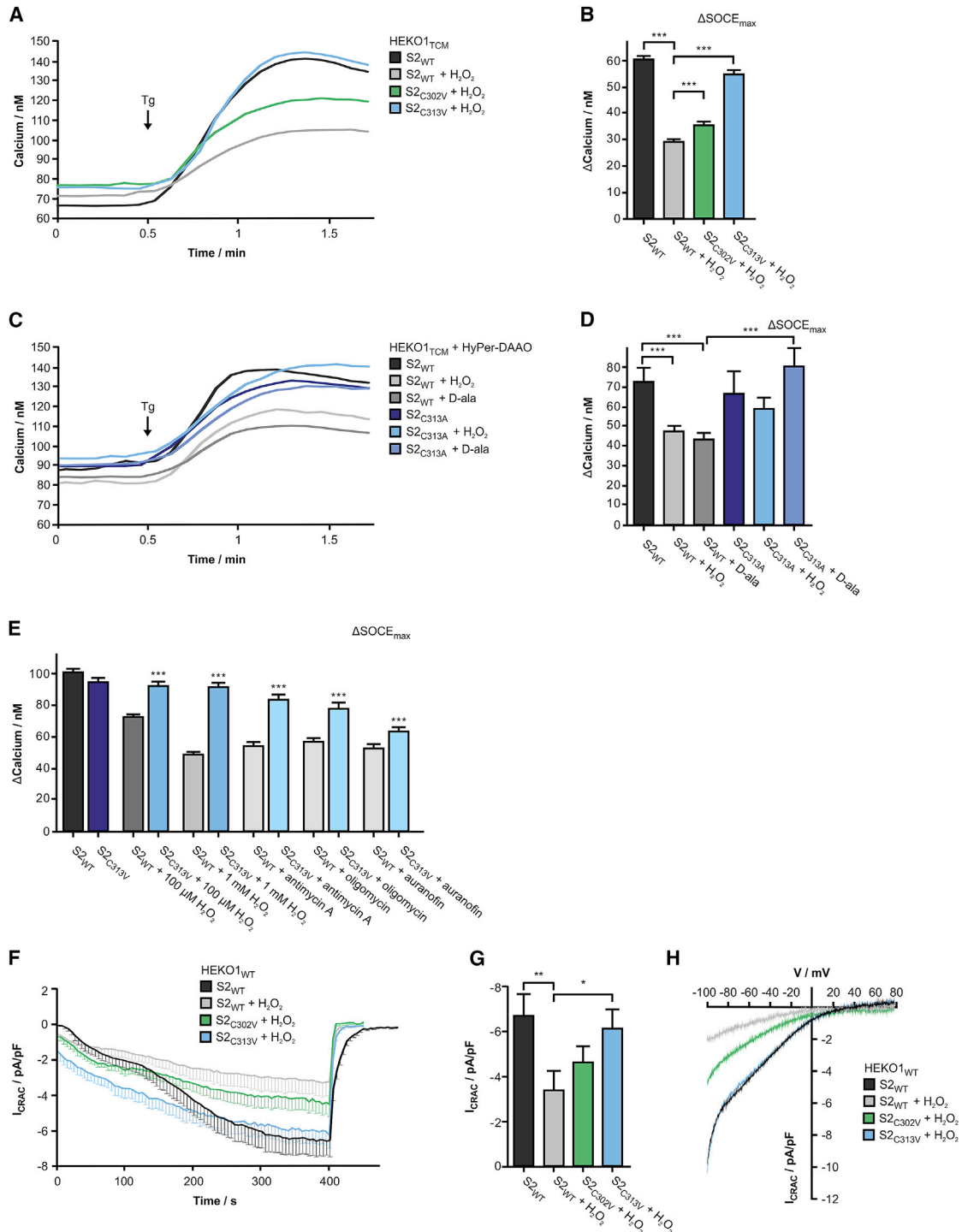
Figure 3. STIM2 C313 Controls the Oxidation-Induced Inhibition of SOCE and I_{CRAC}

(A) Ca^{2+} imaging of HEKO1$_{TCM}$ with transient overexpression of S2$_{WT}$, S2$_{C302V}$, or S2$_{C313V}$ with or without pre-treatment with H_2O_2 (1 mM, 15 min).

(B) Corresponding quantification of $\Delta SOCE_{max}$ (max-basal). Data are presented as mean ± SEM (n values: S2$_{WT}$ = 939, S2$_{WT}$+H_2O_2 = 620, S2$_{C302V}$+H_2O_2 = 432, S2$_{C313V}$+H_2O_2 = 812).

(C) Ca^{2+} imaging of HEKO1$_{TCM}$ with transient overexpression of S2$_{WT\Delta K}$ or S2$_{C313A\Delta K}$ and HyPer-DAAO with or without pre-treatment with H_2O_2 (1 mM, 15 min) or D-ala (4 mM, 60 min).

(D) Corresponding quantification of $\Delta SOCE_{max}$. Data are presented as mean ± SEM (n values: S2$_{WT\Delta K}$ = 24, S2$_{WT\Delta K}$+H_2O_2 = 42, S2$_{WT\Delta K}$+D-ala = 82, S2$_{C313A\Delta K}$ = 33, S2$_{C313A\Delta K}$+H_2O_2 = 35, S2$_{C313A\Delta K}$+D-ala = 71).

(legend continued on next page)

oxidative stress affect STIM2-controlled SOCE. For this purpose, we first transfected HEKO1$_{TCM}$ cells with the HyPer-DAAO construct and measured Tg-induced SOCE with and without D-alanine stimulation. As seen in Figures 3C and 3D, D-alanine treatment caused inhibition of SOCE in HEKO1$_{TCM}$+S2$_{WT}$ cells. Notably, this D-alanine-induced SOCE inhibition was reversed in cells overexpressing the STIM2$_{C313A}$ mutant. To calculate the amount of H$_2$O$_2$ generated by the HEKO1$_{TCM}$ HyPer-DAAO-overexpressing cells, we first measured HyPer fluorescence following stimulation with D-alanine. As seen in Figures S3A and S3B, this induced a significant increase in basal cytosolic H$_2$O$_2$ levels, comparable to the one in melanoma cells. To determine the relative intracellular H$_2$O$_2$ concentration in this experimental setup (4 mM D-alanine for 60 min), we treated the HEKO1$_{TCM}$ HyPer-DAAO cells with increasing concentrations of external H$_2$O$_2$. We found that around 100 μM H$_2$O$_2$ saturates the HyPer biosensor and that the increase in intracellular H$_2$O$_2$ strongly depends on the extracellular H$_2$O$_2$ concentration (Figures S3A and S3C). Based on this calibration, we also estimated that 4 mM D-alanine can induce cumulative intracellular H$_2$O$_2$ levels that correspond to the concentration induced by the addition of around 5.6 μM external H$_2$O$_2$, thus indicating that lower concentrations of the oxidant inhibit SOCE via oxidation of STIM2.

Drugs that block the mitochondrial electron transfer chain (ETC) are known to induce elevated mitochondrial ROS production and can cause oxidative stress by exhausting antioxidant protection in the cytosol, similar to drugs that directly suppress the cellular antioxidant system. Hence, we treated HEKO1$_{TCM}$+S2$_{WT/C313V}$ cells with inhibitors of the mitochondrial ETC, such as oligomycin and antimycin A, and with a drug that inhibits antioxidant enzymes such as thioredoxin reductase (auranofin), and we measured SOCE using the same protocol as in Figure 3A. The quantification of ΔSOCE$_{max}$ (Figure 3E) showed that all three drugs, as well as H$_2$O$_2$, inhibited SOCE in HEKO1$_{TCM}$+S2$_{WT}$ cells. Again, the inhibitory effects were reversed in HEKO1$_{TCM}$ cells overexpressing the S2$_{C313V}$ mutant.

To further dissect the STIM2-controlled redox regulation, we used whole-cell Ca^{2+} current measurements and recorded I$_{CRAC}$. To avoid side effects that may affect SOCE and cause unspecific oxidation of plasma-membrane-bound proteins following external stimulation with H$_2$O$_2$, we applied the oxidant via the patch pipette. I$_{CRAC}$ was induced by adding 20 mM EGTA (disodium ethylenediaminetetraacetate dihydrate) in the pipette solution. As shown in Figures S3D and S3E, HEKO1$_{WT}$ cells transiently overexpressing S2$_{WT}$, S2$_{C302V}$, or S2$_{C313V}$ developed typical and comparable I$_{CRAC}$. However, the addition of H$_2$O$_2$ in the pipette

caused a strong reduction of I$_{CRAC}$ in the HEKO1$_{WT}$+S2$_{WT}$ cells (gray) (Figures 3F–3H). This inhibition was only partially and not significantly reversed in the HEKO1$_{WT}$+S2$_{C302V}$ cells (compare green to gray traces) and was almost fully reversed in the HEKO1$_{WT}$+S2$_{C313V}$ cells (compare blue to gray).

In summary, Ca^{2+} imaging experiments and patch-clamp recordings indicated that C313 is the main redox sensor of STIM2 and that various conditions that cause cellular oxidative stress inhibit STIM2-controlled SOCE through its oxidation.

The CC1-Controlled STIM2 Intramolecular Clamp Is Not Involved in the Oxidation-Induced Inhibition of SOCE

We next aimed to identify the molecular mechanism by which oxidation of C313 affects STIM2 function and inhibits SOCE. The STIM activation cascade is initiated by depletion of ER Ca^{2+} stores and involves STIM oligomerization, its elongation, and binding to ORAI1. Accordingly, several molecular mechanisms underlying the STIM2-controlled SOCE redox regulation were plausible. Oxidation of C313 could (1) prevent opening of the CC1-controlled intramolecular clamp, (2) hinder STIM2-STIM2 (or STIM2-STIM1) cytosolic dimerization, and/or (3) inhibit STIM2-ORAI1 interaction.

To test the first hypothesis, we performed fluorescence resonance energy transfer (FRET) measurements as described in Muik et al. (2009). For this purpose, the cytosolic domain of STIM2 (residues 237–478) was labeled with YFP (at the N terminus) and CFP (at the C terminus). This construct, named OASF2 (see also Figure 1A), was overexpressed in HEK293 cells, and CFP-YFP FRET was recorded in bath solution containing 2 mM external Ca^{2+}. As depicted in Figure 4A, a high FRET signal would suggest an inactive STIM2 conformation, whereas a low FRET signal would mean an open, i.e., extended, conformation. Our results (Figure 4B, upper panels, and Figure 4C) show that the FRET ratio for OASF2 is approximately 0.193, suggesting a rather open state when compared with OASF1 (Fahrner et al., 2014) (FRET for OASF1 = 0.27) and confirming previous findings (Subedi et al., 2018). As seen in Figure 4B (lower panels) and Figure 4C, addition of H$_2$O$_2$ caused a decrease in the CFP-YFP FRET signal, suggesting that oxidation might induce additional extension of OASF2. To test the role of C313, we used the same approach as in Figure 4B in OASF2$_{C313V}$-overexpressing cells. Figures 4D and 4E show that replacing C313 slightly reduced the resting FRET signal when compared with OASF2$_{WT}$, suggesting an additional extended configuration. In addition, the C313 mutant of OASF2 was less effected by H$_2$O$_2$ and resulted in a smaller additional extended configuration in comparison to OASF2$_{WT}$.

(E) Quantification of ΔSOCE$_{max}$ of HEKO1$_{TCM}$ with transient overexpression of S2$_{WT}$ or S2$_{C313V}$ with or without H$_2$O$_2$ pre-treatment (100 μM or 1 mM, 15 min), antimycin A (1 μM, 60 min), oligomycin (1 μM, 60 min), and auranofin (1 μM, 60 min). Data are presented as mean ± SEM (n values: S2$_{WT}$ = 939, S2$_{WT}$+100 μM H$_2$O$_2$ = 966, S2$_{WT}$+1 mM H$_2$O$_2$ = 620, S2$_{WT}$+antimycinA = 286, S2$_{WT}$+oligomycin = 244, S2$_{WT}$+auranofin = 278, S2$_{C313V}$ = 754, S2$_{C313V}$+100 μM H$_2$O$_2$ = 460, S2$_{C313V}$+1 mM H$_2$O$_2$ = 812, S2$_{313V}$+antimycinA = 332, S2$_{C313V}$+oligomycin = 198, S2$_{C313V}$+auranofin = 223).

(F–H) I$_{CRAC}$ in HEK293 cells transiently overexpressing O1$_{WT}$ and S2$_{WT}$, S2$_{C302V}$, or S2$_{C313V}$. (F) Current response in the presence and absence of H$_2$O$_2$ (100 μM) in the pipette solution. I$_{CRAC}$ was blocked with La^{3+} (10 μM) at the end of the measurement. (G) Corresponding quantification of peak currents. (H) Current-voltage (I-V) plots of I$_{CRAC}$ recorded in response to 100 ms voltage ramps ranging from −100 to 80 mV. Data are presented as mean ± SEM (n values: S2$_{WT}$ = 10, S2$_{WT}$+H$_2$O$_2$ = 12, S2$_{C302V}$+H$_2$O$_2$ = 7, S2$_{C313V}$+H$_2$O$_2$ = 11).

Statistical significance was addressed using unpaired, two-tailed Student's t test, *p < 0.05, **p < 0.01, ***p < 0.005. See also Figures S2 and S3. S2$_{WT}$ and S2$_{WT}$+H$_2$O$_2$ data are also shown in Figures 1I and 1J and in (A) and (B); S2$_{313V}$+H$_2$O$_2$ is shown in (B).
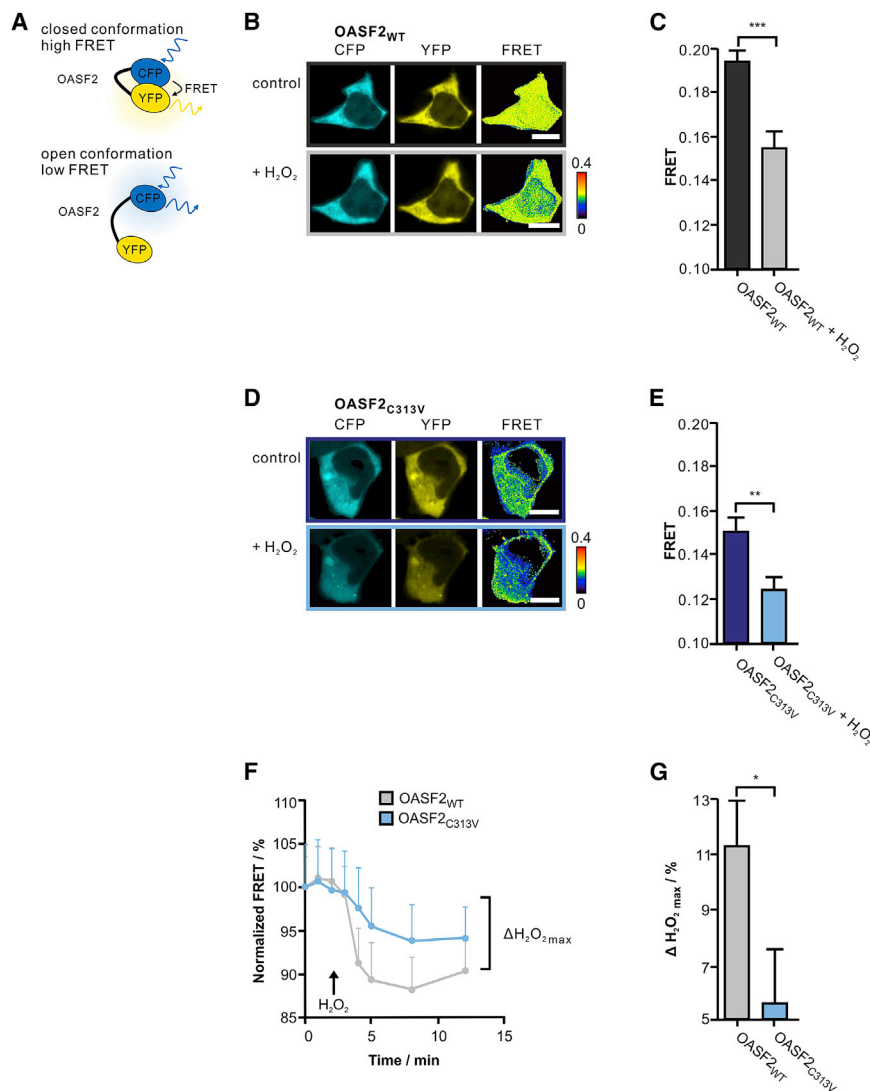
Figure 4. Oxidation of C313 Does Not Control Opening of the OASF2 Fragment

(A) Schematic representation of CFP-YFP FRET measurements based on the OASF2 fragment. Upper panel: closed/folded conformation with positive FRET. Lower panel: open conformation with no FRET.

(B) Representative images of CFP, YFP, and FRET of HEK293 cells overexpressing OASF2$_{WT}$ before and after treatment with H$_2$O$_2$ (100 μM).

(C) Corresponding quantification.

(D) Representative images for OASF2$_{C313V}$.

(E) Corresponding quantification.

(F) Normalized FRET over time (FRET$_{+H2O2}$ − FRET$_{-H2O2}$, normalized to t = 0 min) for OASF2$_{WT}$ and OASF2$_{C313V}$.

(G) Change of FRET after oxidation with H$_2$O$_2$ (100 μM), as indicated in (F) (ΔH$_2$O$_{2max}$ as a percentage).

Data are presented as mean ± SEM (n values: S2$_{WT}$ = 11, S2$_{WT}$+H$_2$O$_2$ = 9, S2$_{C313V}$ = 10, S2$_{C313V}$+H$_2$O$_2$ = 11; scale bars: 10 μm). Statistical significance was addressed using unpaired, two-tailed Student's t test, *p < 0.05, **p < 0.01, ***p < 0.005. See also Figure S4.

CC1 domain plays an important role in STIM-STIM interaction and STIM puncta formation (Fahrner et al., 2014; Prakriya and Lewis, 2015). To test whether oxidation of C313 affects STIM2 activation and evaluate the effect of C313 oxidation on a molecular scale, we performed atomistic molecular dynamics (MD) simulations of a homology model of STIM2 containing the residues 306–391, which is based on the nuclear magnetic resonance (NMR) structure of STIM1 (Stathopulos et al., 2013) (sequence alignment in Figure S5A). One monomer of the NMR structure of STIM1, and therefore of the homology model of STIM2, consists of a C-terminal part of the CC1 domain and the CC2 domain (CC1α3-CC2) that intertwine with each other into a homodimeric conformation (Figure 5A). The CC1α3-CC2 homodimer was simulated four times each (for 500 ns) with C313 either in its non-sulfonylated form (C313) or in its sulfonylated (oxidized) form (C313-Sulf). At the end of the simulations, both the C313 and the C313-Sulf dimers displayed similar overall deviations of 4–8 Å (root-mean-square deviations [RMSD]) from their initial conformation (Figures S5B and S5C). However, the C313-Sulf monomers showed increased flexibility compared with the C313 monomers, especially at the N-terminal end, including C313-Sulf (residues 306–314) and the linker (residues 343–350) that connects the two α helices (Figure 5B). This increased flexibility of the linker region of C313-Sulf is related to a reduced interaction between E314 located in the N-terminal part of one monomer and R342 residing near the turn region of the other monomer, which form a stable salt bridge in the C313 dimer

To compare the effects of H$_2$O$_2$ on OASF2$_{WT}$ and with those on OASF2$_{C313V}$, we subtracted the traces without H$_2$O$_2$ (to correct for bleaching), normalized the starting value (t = 0 min) to 100% (Figure 4F), and calculated the percentage of inhibition. Figure 4G indicated that OASF2$_{WT}$ was more sensitive to oxidation than OASF2$_{C313V}$. Similar results were obtained using OASF2$_{C302V}$ (Figure S4). Nevertheless, these findings could not explain the mechanism responsible for SOCE inhibition following oxidation of STIM2, given that enhanced OASF2 elongation would instead cause elevated SOCE. Accordingly, we set out to test the possible alternatives.

Oxidation of C313 Hinders STIM2 Activation

Activated STIM protein dimers undergo a conformational change and oligomerize, i.e., form puncta close to the plasma membrane, wherein they, in their open conformation, interact with ORAI channels and activate SOCE (Gudlur et al., 2020; Soboloff et al., 2012). It has been demonstrated that the STIM
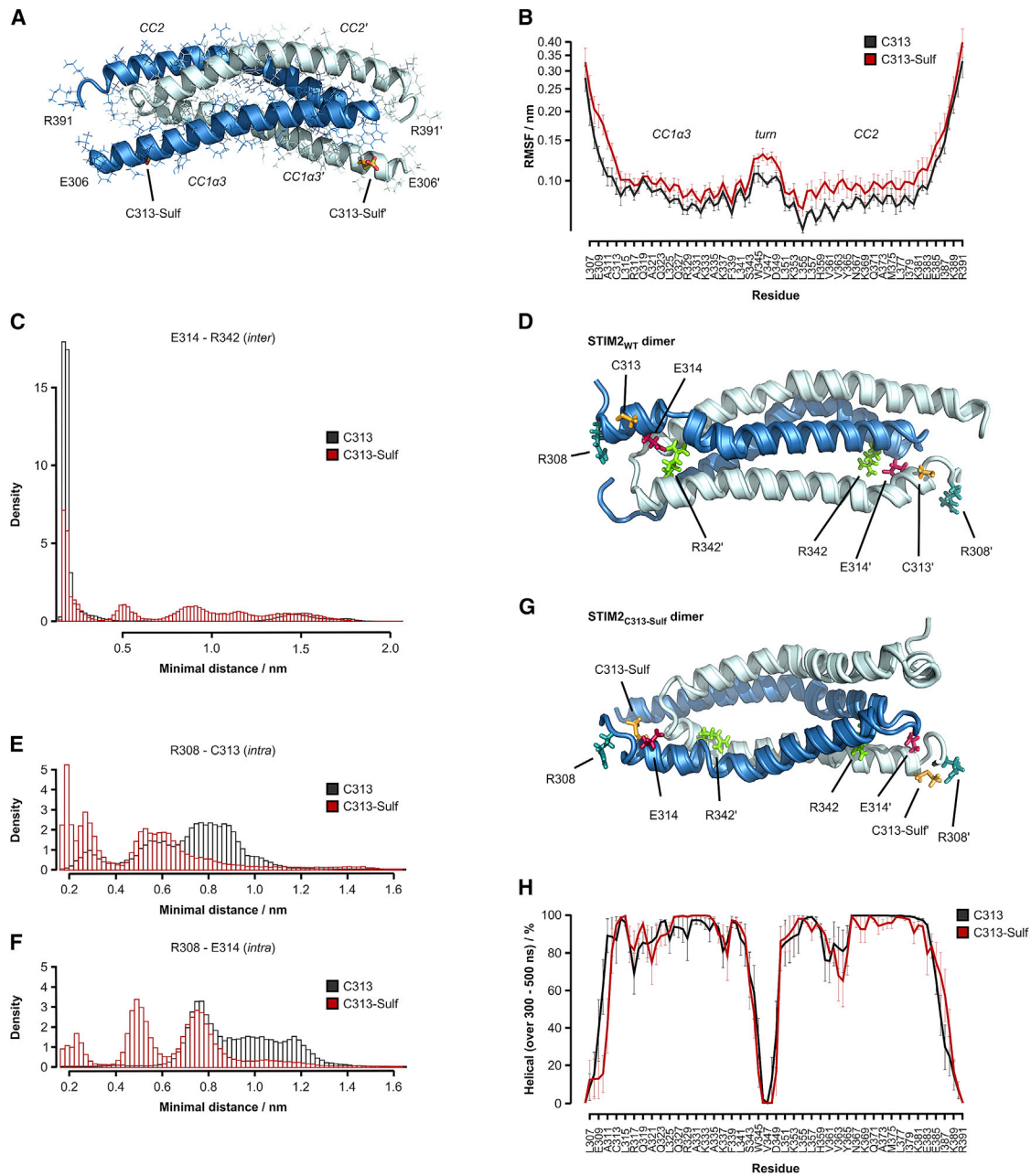
Figure 5. Oxidation of C313 Increases Helical Flexibility and Abolishes an Intermolecular Salt Bridge in STIM2-STIM2 Dimers
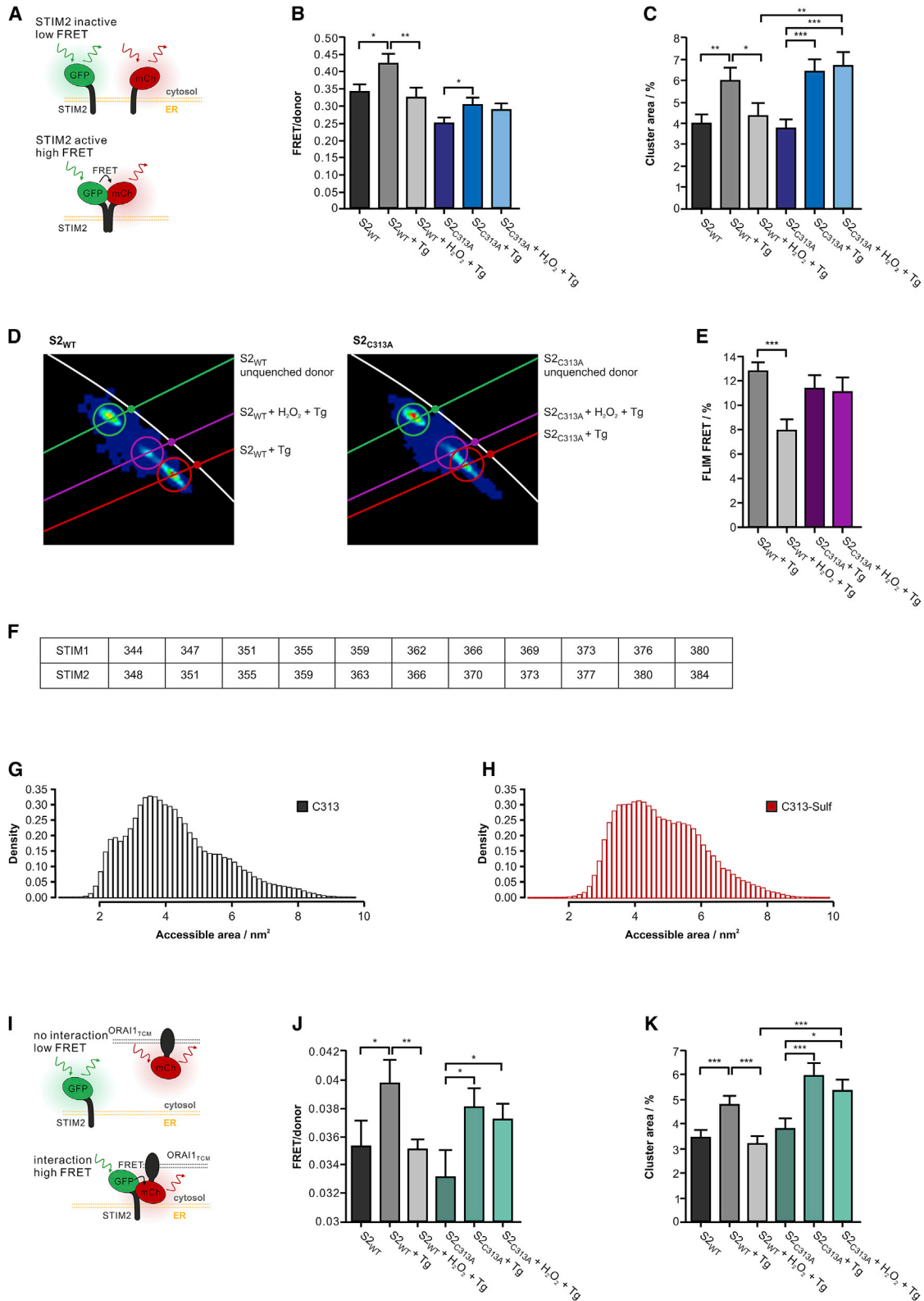
(A) Homology model of human STIM2 CC1α3-CC2. The STIM2 dimer comprises residues E306-R391 in each monomer that form two alpha helices connected by a turn. C313-Sulf is shown as yellow sticks.

(B) STIM2 dimer flexibility in MD simulations. The root-mean-square fluctuations (RMSFs) were calculated as described in STAR Methods. Bars represent the error for the RMSFs of eight individual STIM2 CC1α3-CC2 monomers.

(C–G) Inter- and intramolecular residue-residue interactions within STIM2 CC1α3-CC2. (C) Pairwise minimal distances between E314 of one monomer and R342 of the other monomer were calculated for the C313 and C313-Sulf dimer simulations and are depicted in a histogram. (D) Snapshot of the protein conformation of a C313 dimer simulation (R308, blue-green; C313, yellow; E314, red; R342, green). (E) Pairwise minimal distances between R308 and C313 or C313-Sulf of the same monomer. (F) Pairwise minimal distances between R308 and E314 in the same monomer within C313 or C313-Sulf. (G) Snapshot of a C313-Sulf simulation (R308, blue-green; C313-Sulf, yellow; E314, red; R342, green). The intermolecular E314-R342 salt bridge is broken.

(H) Average helicity for STIM2 CC1α3-CC2 for the C313 simulations (black) and the C313-Sulf simulations (red).

Data are presented as mean ± SEM of both STIM2 CC1α3-CC2 monomers in all simulations. The first and last residues (E306 and R391) are defined as coil by default. See also Figure S5.

A

STIM2 inactive
low FRET

GFP   mCh
                    cytosol
STIM2   ER

STIM2 active
high FRET

       FRET
GFP mCh

STIM2

B

FRET/donor

* **

*

S2$_{WT}$
S2$_{WT}$ + Tg
S2$_{WT}$ + H$_2$O$_2$ + Tg
S2$_{C313A}$
S2$_{C313A}$ + Tg
S2$_{C313A}$ + H$_2$O$_2$ + Tg

C

Cluster area / %

** *
**
***
***

S2$_{WT}$
S2$_{WT}$ + Tg
S2$_{WT}$ + H$_2$O$_2$ + Tg
S2$_{C313A}$
S2$_{C313A}$ + Tg
S2$_{C313A}$ + H$_2$O$_2$ + Tg

D

S2$_{WT}$

S2$_{WT}$ unquenched donor
S2$_{WT}$ + H$_2$O$_2$ + Tg
S2$_{WT}$ + Tg

S2$_{C313A}$

S2$_{C313A}$ unquenched donor
S2$_{C313A}$ + H$_2$O$_2$ + Tg
S2$_{C313A}$ + Tg

E

FLIM FRET / %

***

S2$_{WT}$ + Tg
S2$_{WT}$ + H$_2$O$_2$ + Tg
S2$_{C313A}$ + Tg
S2$_{C313A}$ + H$_2$O$_2$ + Tg

F

STIM1	344	347	351	355	359	362	366	369	373	376	380
STIM2	348	351	355	359	363	366	370	373	377	380	384

G

Density

C313

Accessible area / nm^2

H

Density

C313-Sulf

Accessible area / nm^2

I

no interaction
low FRET

ORAI1$_{TCM}$

GFP   mCh

STIM2   cytosol
            ER

interaction
high FRET

       FRET   ORAI1$_{TCM}$
GFP mCh
            cytosol
STIM2   ER

J

FRET/donor

* **

*
*

S2$_{WT}$
S2$_{WT}$ + Tg
S2$_{WT}$ + H$_2$O$_2$ + Tg
S2$_{C313A}$
S2$_{C313A}$ + Tg
S2$_{C313A}$ + H$_2$O$_2$ + Tg

K

Cluster area / %

*** ***
***
***
*

S2$_{WT}$
S2$_{WT}$ + Tg
S2$_{WT}$ + H$_2$O$_2$ + Tg
S2$_{C313A}$
S2$_{C313A}$ + Tg
S2$_{C313A}$ + H$_2$O$_2$ + Tg

(legend on next page)

simulations (Figures 5C and 5D). In the C313-Sulf simulations, the intermolecular E314-R342 salt bridge breaks and thus destabilizes the CC1α3-CC2 linker (compare Figures 5D and 5G). Moreover, E314 and in particular the neighboring C313-Sulf are instead more frequently involved in an interaction with the neighboring R308 of the same monomer (Figures 5E–5G). Thereby, the first residues of CC1α3 lose their initial helical conformation. On average, the N-terminal part (residues 307–314) in the C313 simulations is ~61% helical, whereas in the C313-Sulf simulations, the helicity is reduced by ~15% (Figure 5H). Moreover, the destabilized CC1α3-CC2 domain induced by C313-Sulf is in line with a slightly extended configuration of the OASF2$_{C313V}$ (Figure 4D). This *in silico* analysis indicated that even in its resting, ORAI-unbound conformation, STIM2 C313 sulfonylation affects the structural properties of the STIM2 dimer.

Our results based on MD simulations suggest that oxidized C313 may destabilize the interaction sites between CC1 and CC2 helices of STIM2. This structural instability may interfere with the CC1-CC1 and/or CC1-CC2 interaction following STIM2 activation. To experimentally test this hypothesis, we performed FRET microscopy of STIM2 (Figure 6A). To prevent the known pre-clustering of STIM2$_{WT}$ (Brandman et al., 2007; Emrich et al., 2019), we used constructs missing the membrane-tethering polybasic Lys-rich domain (STIM2ΔK) (for details, see Brandman et al., 2007). We transfected HEKO1$_{WT}$ cells with STIM2$_{WTΔK-GFP}$+STIM2$_{WTΔK-mCherry}$ or STIM2$_{C313AΔK-GFP}$+STIM2$_{C313AΔK-mCherry}$ and evaluated intermolecular FRET/donor ratio values, as well as the STIM2 cluster-covered area. The data in Figures 6B and 6C show an expected increase of the STIM2$_{WTΔK}$−STIM2$_{WTΔK}$ FRET signal, as well as the STIM2$_{WTΔK}$ cluster-covered area, in cells activated with Tg (black versus gray). Moreover, the Tg-induced increase in FRET efficiency and the cluster-covered area was abolished by H$_2$O$_2$ treatment (gray versus light gray). In addition, we found that Tg treatment increased FRET and the cluster area in cells overexpressing STIM2$_{C313AΔK}$ (dark blue versus blue). However, in these cells, H$_2$O$_2$ treatment did not reduce the Tg-induced increase in FRET and the STIM2 cluster-covered area (blue versus light blue) (Figures 6B and 6C). To elucidate the mechanism by which oxidation of C313 affects STIM2 interaction, we employed fluorescence lifetime imaging microscopy (FLIM), because it

is among the most accurate methods for measuring intermolecular interactions via FRET. STIM2$_{WTΔK-GFP}$ was used as a fluorescence donor, and STIM2$_{WTΔK-mCherry}$ was used as an acceptor. Initially, using a bi-exponential curve fit, we identified two lifetimes for GFP: a shorter one ($\tau_1 = 1.25 \pm 0.16$ ns) and a longer one ($\tau_2 = 2.28 \pm 0.05$ ns). To evaluate the effects of STIM2 redox regulation and the role of its C313 on GFP lifetimes, we treated the STIM2$_{WTΔK}$- and STIM2$_{C313AΔK}$-overexpressing HEKO1$_{WT}$ cells with H$_2$O$_2$ and Tg. These data were processed using the phasor analysis method, because it has proved to be a robust approach for the identification of different molecular species based on their lifetimes, as well as for the estimation of FRET efficiency of molecular species exhibiting multi-exponential decays (for technical details, see Digman et al., 2008). The phasor plots shown in Figure 6D indicate that the unquenched donors (green circle; STIM2$_{WTΔK-GFP}$, left panel; and STIM2$_{C313AΔK-GFP}$, right panel) exhibit point clouds with the longest averaged lifetimes. The shortest donor lifetimes were recorded in HEKO1$_{WT}$ cells treated with Tg only in STIM2$_{WTΔK}$- and STIM2$_{C313AΔK}$-overexpressing cells (red circles). Hydrogen peroxide treatment prevented Tg-induced lifetime reduction of STIM2$_{WTΔK}$ (cyan circle, left panel). However, in the STIM2$_{C313AΔK}$-expressing cells, this H$_2$O$_2$-induced prolongation of donor lifetime was diminished (cyan circles, right panel) when compared with STIM2$_{WT}$. In addition to donor lifetimes, we quantified FRET efficiency using the FRET trajectory approach as part of phasor analysis (Digman et al., 2008). The quantification of this analysis is shown in Figure 6E and displays a similar pattern as the FRET/donor ratio-based analysis shown in Figure 6B.

Altogether, FRET and FLIM of STIM2 confirmed the importance of C313 redox regulation and suggested that oxidation of STIM2$_{C313}$ interferes with STIM2-STIM2 interaction following its activation.

Oxidation of C313 Does Not Affect STIM2-ORAI1 Interaction

The previous results indicated that oxidation, i.e., S-sulfonylation, of C313 hinders STIM2 oligomerization. However, these findings did not exclude the possibility that oxidized C313 might also affect STIM2 interaction with ORAI1. To evaluate this hypothesis, we used MD simulations and calculated the solvent-

Figure 6. STIM2-STIM2 Interaction Is Diminished by Redox Modifications of C313

(A) Schematic representation of STIM2-STIM2 FRET measurements.

(B and C) Confocal microscopy of HEKO1$_{WT}$ cells overexpressing S2$_{WTΔK}$ or S2$_{C313AΔK}$ fused to GFP and mCherry treated with Tg (1 μM) or H$_2$O$_2$ (100 μM) and Tg before fixation. (B) Cluster FRET/donor ratio. (C) Cluster area normalized to cell area. Data are presented as mean ± SEM (n values: S2$_{WT}$ = 68, S2$_{WT}$+Tg = 110, S2$_{WT}$+H$_2$O$_2$+Tg = 78, S2$_{C313A}$ = 62, S2$_{C313A}$+Tg = 83, S2$_{C313A}$+H$_2$O$_2$+Tg = 51).

(D and E) FLIM microscopy of HEKO1$_{WT}$ cells overexpressing S2$_{WTΔK}$ or S2$_{C313AΔK}$ fused to GFP and mCherry. Cells were treated as in (B) and (C).

(D) FLIM-imaging-based phasor plots showing point clouds of the molecular species occurring after the respective treatment.

(E) FRET efficiency calculation (as a percentage) of the FLIM-imaging-based data shown in (D) (n values: S2$_{WT}$+Tg = 10, S2$_{WT}$+H$_2$O$_2$+Tg = 4, S2$_{C313A}$+Tg = 5, S2$_{C313A}$+H$_2$O$_2$+Tg = 10).

(F–H) STIM1/STIM2 residues used to calculate the solvent-accessible surface area (SASA) based on the STIM1-ORAI1 NMR structure (Stathopulos et al., 2013) (Figures S5D and S5E). SASA is shown for equivalent residues in STIM2 in simulations (calculated over 300–500 ns) for (G) C313 and (H) C313-Sulf.

(I) Schematic representation of STIM2-ORAI1$_{TCM}$ FRET measurements.

(J and K) Confocal microscopy of HEK293 cells overexpressing S2$_{WTΔK⁻GFP}$ or S2$_{C313AΔK-GFP}$ and mCherry-ORAI1$_{TCM}$ treated with Tg (1 μM) or H$_2$O$_2$ (100 μM) and Tg before fixation. (J) Cluster FRET/donor ratio. (K) Cluster area normalized to cell area. Data are presented as mean ± SEM (n values: S2$_{WT}$ = 113, S2$_{WT}$+Tg = 119, S2$_{WT}$+H$_2$O$_2$+Tg = 110, S2$_{C313A}$ = 68, S2$_{C313A}$+Tg = 118, S2$_{C313A}$+H$_2$O$_2$+Tg = 109).

Statistical significance was addressed using unpaired, two-tailed Student's t test, *p < 0.05, **p < 0.01, ***p < 0.005.

accessible surface area (SASA) of the residues that form the ORAI1 binding site in the NMR structures of STIM1 with bound ORAI1 C termini (Figure S5D; SASA = 8.02 nm^2) and without bound ORAI1 C termini (Figure S5E; SASA = 2.54 nm^2) (Stathopulos et al., 2013). Then, we compared them to the surface area of the equivalent residues in STIM2 C313 and C313-Sulf obtained in the simulations (Figures 6F–6H). Our data indicated that the binding sites overall become more accessible in the C313 simulations (SASA = 4.4 ± 1.4 nm^2) and C313-Sulf simulations (SASA = 4.8 ± 1.2 nm^2) compared with the STIM1 apo structure, with the distributions of the accessible surface areas marginally shifted toward larger values for C313-Sulf compared with C313 dimer simulations (compare Figures 6G and 6H). These simulations thus suggested that oxidation of C313 would most likely not disturb STIM2-ORAI1 interaction. To test this experimentally, we performed FRET imaging and cluster-size analyses in HEK293 cells expressing STIM2$_{WT\Delta K}$-GFP and mCherry-ORAI1$_{TCM}$ (Figure 6I) with and without stimulation with Tg. Our results showed an increase of the STIM2$_{WT\Delta K}$-ORAI1$_{TCM}$ FRET signal, as well as the STIM2$_{WT\Delta K}$-ORAI1$_{TCM}$ cluster-covered area, in cells activated with Tg (black versus gray). We also found that H$_2$O$_2$ treatment suppressed the Tg-induced increase in FRET efficiency and the cluster-covered area (gray versus light gray). In addition, Tg treatment increased FRET and the cluster area in cells overexpressing STIM2$_{C313A\Delta K}$-ORAI1$_{TCM}$ (dark green versus green). However, in these cells, H$_2$O$_2$ treatment did not reduce the Tg-induced increase in FRET and the STIM2$_{WT}$-ORAI1$_{WT}$ cluster-covered area (green versus light green, Figures 6J and 6K). Given that this finding was similar to the one for STIM2-STIM2 (Figures 6B and 6C), we postulated that the STIM2-ORAI1 interaction under oxidative stress is most likely controlled by the redox control of STIM2 oligomerization.

In summary, the MD simulations and the FRET imaging suggested that if the STIM2-STIM2 interaction would not have been affected, the ORAI1-STIM2 interaction would have most likely not been overtly altered by STIM2$_{C313}$ oxidation. Hence, we could conclude that the oxidation of C313 inhibits SOCE mostly by hindering STIM2-STIM2 clustering, i.e., interaction.

DISCUSSION

SOCE is a Ca^{2+} entry mechanism that is highly sensitive to redox modifications (Bogeski and Niemeyer, 2014; Nunes and Demaurex, 2014). We reported SOCE redox regulation even before the molecular identity of STIM and ORAI was fully elucidated (Bogeski et al., 2006). Moreover, we demonstrated that extracellular oxidants cause oxidative modifications of C195 in ORAI1 and ORAI2 and thereby inhibit SOCE (Bogeski et al., 2010). We also found that ORAI3 lacks the C195 and is thereby redox insensitive (Bogeski et al., 2010). Accordingly, we demonstrated that the ORAI3/ORAI1 ratio determines the overall CRAC channel redox sensitivity and thus controls monocyte immune responses (Saul et al., 2016; Schmidt et al., 2019). Moreover, in a recent study, redox regulation of ORAI channels was shown to be involved in the mitochondrial control of SOCE (Ben-Kasus Nissim et al., 2017). In addition to ORAI, STIM1 function can be redox regulated. A mature STIM1 protein has four cysteine residues: two in

the ER lumen, one in the ER transmembrane domain, and one in the cytosolic CAD/SOAR domain (Figure 1A). The role of these cysteines was examined in the context of redox regulation, and it was demonstrated that S-glutathionylation of the luminal C56 causes Ca^{2+} store-independent clustering of STIM1 and thus activation of ORAI channels (Hawkins et al., 2010). Another study showed that STIM1 function is regulated by the ER oxidoreductase ERp57 via redox modulation of C49 and C56. The lack of these two residues caused inhibition of SOCE, whereas ERp57 knockdown caused its elevation (Prins et al., 2011). Furthermore, studies have demonstrated that S-nitrosylation of STIM1 C49 and C56 interferes with STIM1 oligomerization and consequently leads to SOCE inhibition (Gui et al., 2018; Zhu et al., 2018).

In this study, we evaluated the redox regulation of STIM2. As seen in Figure 1A, STIM2 has ten additional cytosolic cysteines compared with STIM1, but their role was not yet understood. Our redox proteomic analysis identified two of these cysteines (C302 and C313), localized in the CC1 domain of STIM2, to be oxidized following treatment with external oxidants. The conserved cysteines within the lumen of the ER, shown previously to be regulated in STIM1 (described earlier), were identified neither in our analysis nor in an *in vivo* redox proteomic study (Xiao et al., 2020). These findings do not negate the role of the STIM2 luminal cysteines in SOCE redox regulation but rather suggest that oxidative stress needs to be discussed as a localized subcellular event, not as a generalized state of a cell (Mishina et al., 2019). In terms of SOCE, spatially limited, i.e., local, redox regulation would be physiologically plausible. The ORAI/STIM machinery spans from the extracellular space to the ER lumen, thereby crossing the plasma membrane, the cytosol, and the ER membrane. At physiological conditions, the redox potential of all three compartments (ER lumen, cytosol, and extracellular space) is different. The cytosol is rather reducing, whereas the ER lumen is highly oxidizing (Sies et al., 2017). This suggests that the exact intracellular localization of cysteines in ORAI and STIM could play a decisive role in determining the CRAC channel function under conditions that cause oxidative stress. Based on the current knowledge, elevated oxidative burden in the extracellular space and in the cytosol would cause inhibition of SOCE, whereas elevation in the oxidizing potential of the ER lumen would cause SOCE activation following S-glutathionylation and SOCE inhibition following S-nitrosylation. Nevertheless, it is also known that alterations of the redox state of one compartment can affect the redox state of another cellular compartment (Appenzeller-Herzog et al., 2016; Bertolotti et al., 2016; Mishina et al., 2019). Determining how these complex redox-signaling mechanisms integrate in the context of STIM and ORAI redox regulation and how this regulation translates into physiology and pathology requires additional comprehensive investigation. In melanoma, for example, cysteine oxidation of ORAI1 and/or STIM2 inhibits SOCE and would thereby block migration and invasion of this highly aggressive cancer. Indeed, studies that demonstrate that antioxidants promote melanoma metastatic spread (Le Gal et al., 2015; Piskounova et al., 2015), together with studies reporting an essential role of ORAI and STIM in melanoma pathobiology (Stanisz et al., 2016), provide a possible connection between SOCE redox regulation and
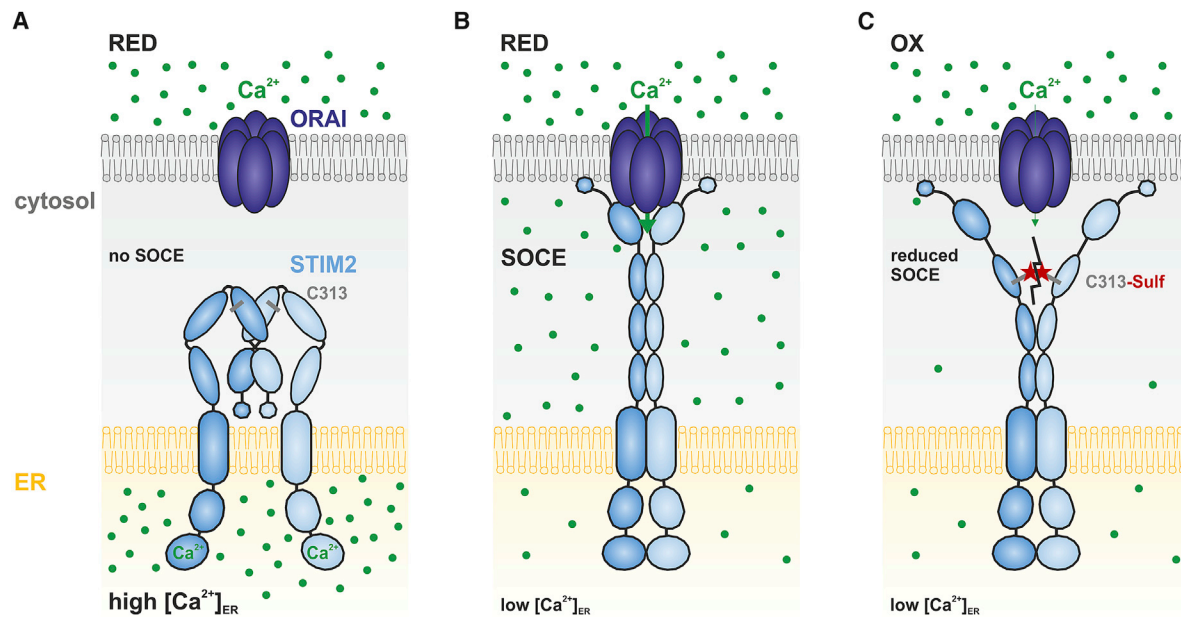
Figure 7. Oxidation of C313 Hinders STIM2 Activation and Inhibits SOCE

(A) Under resting conditions (i.e., high $[Ca^{2+}]_{ER}$), STIM2 is in a closed conformation. ORAI1 channels and SOCE are inactive.

(B) Depletion of the ER Ca^{2+} stores (i.e., low $[Ca^{2+}]_{ER}$) during signaling events (e.g. surface receptor activation) leads to Ca^{2+} dissociation from the STIM2 luminal EF-hands, causing STIM2 dimers to unfold, elongate, and thus activate ORAI channels and SOCE.

(C) Under oxidizing conditions STIM2 C313 is sulfonylated, a modification that hinders proper STIM2 activation and its gating of ORAI1 and subsequently causes SOCE inhibition.

melanoma aggressive behavior. Moreover, a study that performed a comprehensive state-of-the-art redox proteomic analysis of different tissues in young and aged mice identified STIM2 C313 to be oxidized in 9 of 20 samples (Xiao et al., 2020). Thus, this *in vivo* study confirmed our *in vitro* findings and demonstrated that STIM2 oxidative modifications are physiologically highly relevant. Xiao et al. (2020) identified oxidative modifications of four additional cytosolic cysteines. However, the number of conditions in which these cysteines were identified in an oxidized form and the percentage of occupancy were significantly inferior compared with C313 (for details, see Xiao et al., 2020). Again, oxidative modification of the luminal cysteines of STIM2 was not detected.

An NMR-based 3D structure of the whole STIM2 protein, with exception of its EF-SAM domain (Zheng et al., 2011), is not available. We therefore transformed the reported STIM1 NMR structure (Stathopulos et al., 2013) by replacing the different amino acids between STIM1 and STIM2 to generate a homology model that will help us in understanding the role of C313 oxidation in STIM2. The data gained from this model, together with our experimental FRET- and FLIM-obtained results (Figures 5 and 6), indicated that oxidation of C313 inhibits SOCE by interfering with STIM2 activation, i.e., dimerization/oligomerization. In addition, using the same model, we evaluated the role of STIM1 R304 mutation into tryptophan (STIM1-R304W). R304 corresponds to R308 in STIM2, and its R304W mutation renders STIM1 constitutively active, leading to the development of Stormorken syndrome (Misceo et al., 2014). A recent study demonstrated that R304 point mutations in STIM1 caused altered STIM1 CC1α2

and CC1α3 linker flexibility and CC1 homodimerization (Fahrner et al., 2018). This study suggested that the R304W STIM1 mutant increases the CC1 homodimerization and rigidifies the CC1α2-CC1α3 linker by the formation of an α helix, resulting in an extended STIM1 conformation that enables interaction with ORAI. Oxidation of C313 in STIM2 and the coupled interaction of C313-Sulf with R308 will probably also affect the conformation of the linker, and an effect on the transition from the closed to the extended state of STIM2 is likely. However, simulation of a full-length STIM2 structure to shed light on these hypotheses would have been beyond the scope of this study. Future studies are warranted in addressing these important questions and in examining whether and how a mutation or mutations and posttranslational modifications of STIM2 R308 and/or C313 will affect human physiology and pathology.

In this study, we show that under normal (reducing) conditions, depletion of ER Ca^{2+} stores leads to STIM2 elongation, oligomerization, and activation of ORAI channels (Figures 7A and 7B). However, under oxidative stress, the C313 in the CC1 domain of STIM2 will be oxidized. As experimentally demonstrated and depicted in Figure 7C, we found that C313 thiol oxidation interferes with STIM2 activation and leads to inhibition of SOCE.

In summary, we demonstrate that oxidation of a specific cysteine (C313) in STIM2 is an essential redox-controlled regulatory mechanism of cellular Ca^{2+} homeostasis. Tissue-specific STIM2 abundance and local ROS hotspots could thus play a decisive role in oxidative stress-induced pathological conditions such as aging, cancer, cardiovascular disease, and neurodegenerative disorders.

STAR★METHODS

Detailed methods are provided in the online version of this paper and include the following:

-
-
  - ○
  - ○
  - ○
-
  - ○
  - ○
-
  - ○
  - ○
  - ○
  - ○
  - ○
  - ○
  - ○
  - ○
  - ○
  - ○
  - ○
  - ○
  - ○
  - ○
  - ○
  - ○
-

SUPPLEMENTAL INFORMATION

Supplemental Information can be found online at https://doi.org/10.1016/j.celrep.2020.108292.

AUTHOR CONTRIBUTIONS

Conceptualization of the study: I.B. Writing: I.B. and R. Schindl, with help from C.S.G., S.A.K., and R.A.B. Experimental and theoretical data collection and analysis: C.S.G., S.C., R.B., R. Schober, S.A.K., S.G., A.B., Z.B.d.R., D.E., I.S.-T., C.I., D.A., X.Z., A.R., T.L., D.E., M.F., V.L., M.M., I.F., and R.A.B. Supervision: M.A.H., J.M., V.V.B., M.H., R.A.B., R. Schindl, and I.B. Proofreading and editing of the manuscript: all authors.

DECLARATION OF INTERESTS

The authors declare no competing interests.

REFERENCES

Abraham, M.J., Murtola, T., Schulz, R., Páll, S., Smith, J.C., Hess, B., and Lindahl, E. (2015). GROMACS: High performance molecular simulations through multi-level parallelism from laptops to supercomputers. SoftwareX *1–2*, 19–25.

Ambudkar, I. (2018). Calcium signaling defects underlying salivary gland dysfunction. Biochim. Biophys. Acta Mol. Cell Res. *1865* (*11 Pt B*), 1771–1777.

Appenzeller-Herzog, C., Bánhegyi, G., Bogeski, I., Davies, K.J., Delaunay-Moisan, A., Forman, H.J., Görlach, A., Kietzmann, T., Laurindo, F., Margittai, E., et al. (2016). Transit of H2O2 across the endoplasmic reticulum membrane is not sluggish. Free Radic. Biol. Med. *94*, 157–160.

Ben-Kasus Nissim, T., Zhang, X., Elazar, A., Roy, S., Stolwijk, J.A., Zhou, Y., Motiani, R.K., Gueguinou, M., Hempel, N., Hershfinkel, M., et al. (2017). Mitochondria control store-operated Ca^{2+} entry through Na^+ and redox signals. EMBO J. *36*, 797–815.

Benkert, P., Biasini, M., and Schwede, T. (2011). Toward the estimation of the absolute quality of individual protein structure models. Bioinformatics *27*, 343–350.

Berendsen, H.J.C., Postma, J.P.M., van Gunsteren, W.F., DiNola, A., and Haak, J.R. (1984). Molecular dynamics with coupling to an external bath. J. Chem. Phys. *81*, 3684–3690.

Berman, H.M., Westbrook, J., Feng, Z., Gilliland, G., Bhat, T.N., Weissig, H., Shindyalov, I.N., and Bourne, P.E. (2000). The Protein Data Bank. Nucleic Acids Res. *28*, 235–242.

Berna-Erro, A., Braun, A., Kraft, R., Kleinschnitz, C., Schuhmann, M.K., Stegner, D., Wultsch, T., Eilers, J., Meuth, S.G., Stoll, G., and Nieswandt, B. (2009). STIM2 regulates capacitive Ca2+ entry in neurons and plays a key role in hypoxic neuronal cell death. Sci. Signal. *2*, ra67.

Berna-Erro, A., Jardin, I., Salido, G.M., and Rosado, J.A. (2017). Role of STIM2 in cell function and physiopathology. J. Physiol. *595*, 3111–3128.

Bertolotti, M., Farinelli, G., Galli, M., Aiuti, A., and Sitia, R. (2016). AQP8 transports NOX2-generated H2O2 across the plasma membrane to promote signaling in B cells. J. Leukoc. Biol. *100*, 1071–1079.

Bhardwaj, R., Hediger, M.A., and Demaurex, N. (2016). Redox modulation of STIM-ORAI signaling. Cell Calcium *60*, 142–152.

Bogeski, I., and Niemeyer, B.A. (2014). Redox regulation of ion channels. Antioxid. Redox Signal. *21*, 859–862.

Bogeski, I., Bozem, M., Sternfeld, L., Hofer, H.W., and Schulz, I. (2006). Inhibition of protein tyrosine phosphatase 1B by reactive oxygen species leads to maintenance of Ca2+ influx following store depletion in HEK 293 cells. Cell Calcium *40*, 1–10.

Bogeski, I., Kummerow, C., Al-Ansary, D., Schwarz, E.C., Koehler, R., Kozai, D., Takahashi, N., Peinelt, C., Griesemer, D., Bozem, M., et al. (2010). Differential redox regulation of ORAI ion channels: a mechanism to tune cellular calcium signaling. Sci. Signal. *3*, ra24.

Bogeski, I., Kappl, R., Kummerow, C., Gulaboski, R., Hoth, M., and Niemeyer, B.A. (2011). Redox regulation of calcium ion channels: chemical and physiological aspects. Cell Calcium *50*, 407–423.

Brandman, O., Liou, J., Park, W.S., and Meyer, T. (2007). STIM2 is a feedback regulator that stabilizes basal cytosolic and endoplasmic reticulum Ca2+ levels. Cell *131*, 1327–1339.

Bussi, G., Donadio, D., and Parrinello, M. (2007). Canonical sampling through velocity rescaling. J. Chem. Phys. *126*, 014101.

Carrasco, S., and Meyer, T. (2011). STIM Proteins and the Endoplasmic Reticulum-Plasma Membrane Junctions. Annu. Rev. Biochem. *80*, 973–1000.

Cheng, K.T., Alevizos, I., Liu, X., Swaim, W.D., Yin, H., Feske, S., Oh-hora, M., and Ambudkar, I.S. (2012). STIM1 and STIM2 protein deficiency in T lymphocytes underlies development of the exocrine gland autoimmune disease, Sjogren's syndrome. Proc. Natl. Acad. Sci. USA *109*, 14544–14549.

Clemens, R.A., Chong, J., Grimes, D., Hu, Y., and Lowell, C.A. (2017). STIM1 and STIM2 cooperatively regulate mouse neutrophil store-operated calcium entry and cytokine production. Blood *130*, 1565–1577.

Cornell, W.D., Cieplak, P., Bayly, C.I., and Kollman, P.A. (1993). Application of RESP charges to calculate conformational energies, hydrogen bond energies, and free energies of solvation. J. Am. Chem. Soc. *115*, 9620–9631.

Cox, J., and Mann, M. (2008). MaxQuant enables high peptide identification rates, individualized p.p.b.-range mass accuracies and proteome-wide protein quantification. Nat. Biotechnol. *26*, 1367–1372.

Cui, B., Yang, X., Li, S., Lin, Z., Wang, Z., Dong, C., and Shen, Y. (2013). The inhibitory helix controls the intramolecular conformational switching of the C-terminus of STIM1. PLoS ONE *8*, e74735.

Darden, T., York, D., and Pedersen, L. (1993). Particle mesh Ewald: An N·log(N) method for Ewald sums in large systems. J. Chem. Phys. *98*, 10089–10092.

Diercks, B.P., Werner, R., Weidemüller, P., Czarniak, F., Hernandez, L., Lehmann, C., Rosche, A., Krüger, A., Kaufmann, U., Vaeth, M., et al. (2018). ORAI1, STIM1/2, and RYR1 shape subsecond Ca²⁺ microdomains upon T cell activation. Sci. Signal. *11*, eaat0358.

Digman, M.A., Caiolfa, V.R., Zamai, M., and Gratton, E. (2008). The phasor approach to fluorescence lifetime imaging analysis. Biophys. J. *94*, L14–L16.

Emrich, S.M., Yoast, R.E., Xin, P., Zhang, X., Pathak, T., Nwokonko, R., Gueguinou, M.F., Subedi, K.P., Zhou, Y., Ambudkar, I.S., et al. (2019). Cross-talk between N-terminal and C-terminal domains in stromal interaction molecule 2 (STIM2) determines enhanced STIM2 sensitivity. J. Biol. Chem. *294*, 6318–6332.

Fahrner, M., Muik, M., Schindl, R., Butorac, C., Stathopulos, P., Zheng, L., Jardin, I., Ikura, M., and Romanin, C. (2014). A coiled-coil clamp controls both conformation and clustering of stromal interaction molecule 1 (STIM1). J. Biol. Chem. *289*, 33231–33244.

Fahrner, M., Stadlbauer, M., Muik, M., Rathner, P., Stathopulos, P., Ikura, M., Müller, N., and Romanin, C. (2018). A dual mechanism promotes switching of the Stormorken STIM1 R304W mutant into the activated state. Nat. Commun. *9*, 825.

Feske, S., Gwack, Y., Prakriya, M., Srikanth, S., Puppel, S.H., Tanasa, B., Hogan, P.G., Lewis, R.S., Daly, M., and Rao, A. (2006). A mutation in Orai1 causes immune deficiency by abrogating CRAC channel function. Nature *441*, 179–185.

Gales, L., Saraiva, M.J., and Damas, A.M. (2007). Structural basis for the protective role of sulfite against transthyretin amyloid formation. Biochim. Biophys. Acta *1774*, 59–64.

Grynkiewicz, G., Poenie, M., and Tsien, R.Y. (1985). A new generation of Ca2+ indicators with greatly improved fluorescence properties. J. Biol. Chem. *260*, 3440–3450.

Gudlur, A., Zeraik, A.E., Hirve, N., and Hogan, P.G. (2020). STIM calcium sensing and conformational change. J. Physiol. *598*, 1695–1705.

Gui, L., Zhu, J., Lu, X., Sims, S.M., Lu, W.Y., Stathopulos, P.B., and Feng, Q. (2018). S-Nitrosylation of STIM1 by Neuronal Nitric Oxide Synthase Inhibits Store-Operated Ca²⁺ Entry. J. Mol. Biol. *430*, 1773–1785.

Hawkins, B.J., Irrinki, K.M., Mallilankaraman, K., Lien, Y.-C., Wang, Y., Bhanumathy, C.D., Subbiah, R., Ritchie, M.F., Soboloff, J., Baba, Y., et al. (2010). S-glutathionylation activates STIM1 and alters mitochondrial homeostasis. J. Cell Biol. *190*, 391–405.

Hehre, W.J. (1976). *Ab initio* molecular orbital theory. Acc. Chem. Res. *9*, 399–406.

Hogan, P.G., Lewis, R.S., and Rao, A. (2010). Molecular Basis of Calcium Signaling in Lymphocytes: STIM and ORAI. Annu. Rev. Immunol. *28*, 491–533.

Hooper, R., Zhang, X., Webster, M., Go, C., Kedra, J., Marchbank, K., Gill, D.L., Weeraratna, A.T., Trebak, M., and Soboloff, J. (2015). Novel Protein Kinase C-Mediated Control of Orai1 Function in Invasive Melanoma. Mol. Cell. Biol. *35*, 2790–2798.

Hoth, M., and Niemeyer, B.A. (2013). The Neglected CRAC Proteins: Orai2, Orai3, and STIM2. Curr. Top. Membr. *71*, 237–271.

Hoth, M., and Penner, R. (1992). Depletion of intracellular calcium stores activates a calcium current in mast cells. Nature *355*, 353–356.

Kilch, T., Alansary, D., Peglow, M., Dörr, K., Rychkov, G., Rieger, H., Peinelt, C., and Niemeyer, B.A. (2013). Mutations of the Ca2+-sensing stromal interaction molecule STIM1 regulate Ca2+ influx by altered oligomerization of STIM1 and by destabilization of the Ca2+ channel Orai1. J. Biol. Chem. *288*, 1653–1664.

Korzeniowski, M.K., Manjarrés, I.M., Varnai, P., and Balla, T. (2010). Activation of STIM1-Orai1 involves an intramolecular switching mechanism. Sci. Signal. *3*, ra82.

Le Gal, K., Ibrahim, M.X., Wiel, C., Sayin, V.I., Akula, M.K., Karlsson, C., Dalin, M.G., Akyürek, L.M., Lindahl, P., Nilsson, J., and Bergo, M.O. (2015). Antioxidants can increase melanoma metastasis in mice. Sci. Transl. Med. *7*, 308re8.

Leichert, L.I., Gehrke, F., Gudiseva, H.V., Blackwell, T., Ilbert, M., Walker, A.K., Strahler, J.R., Andrews, P.C., and Jakob, U. (2008). Quantifying changes in the thiol redox proteome upon oxidative stress *in vivo*. Proc. Natl. Acad. Sci. USA *105*, 8197–8202.

Lindemann, C., and Leichert, L.I. (2012). Quantitative redox proteomics: the NOxICAT method. Methods Mol. Biol. *893*, 387–403.

Lindemann, C., Lupilova, N., Müller, A., Warscheid, B., Meyer, H.E., Kuhlmann, K., Eisenacher, M., and Leichert, L.I. (2013). Redox proteomics uncovers peroxynitrite-sensitive proteins that help *Escherichia coli* to overcome nitrosative stress. J. Biol. Chem. *288*, 19698–19714.

Liou, J., Fivaz, M., Inoue, T., and Meyer, T. (2007). Live-cell imaging reveals sequential oligomerization and local plasma membrane targeting of stromal interaction molecule 1 after Ca2+ store depletion. Proc. Natl. Acad. Sci. USA *104*, 9301–9306.

Maier, J.A., Martinez, C., Kasavajhala, K., Wickstrom, L., Hauser, K.E., and Simmerling, C. (2015). ff14SB: Improving the Accuracy of Protein Side Chain and Backbone Parameters from ff99SB. J. Chem. Theory Comput. *11*, 3696–3713.

Matlashov, M.E., Belousov, V.V., and Enikolopov, G. (2014). How much H(2)O(2) is produced by recombinant D-amino acid oxidase in mammalian cells? Antioxid. Redox Signal. *20*, 1039–1044.

Misceo, D., Holmgren, A., Louch, W.E., Holme, P.A., Mizobuchi, M., Morales, R.J., De Paula, A.M., Stray-Pedersen, A., Lyle, R., Dalhus, B., et al. (2014). A dominant STIM1 mutation causes Stormorken syndrome. Hum. Mutat. *35*, 556–564.

Mishina, N.M., Bogdanova, Y.A., Ermakova, Y.G., Panova, A.S., Kotova, D.A., Bilan, D.S., Steinhorn, B., Arnér, E.S.J., Michel, T., and Belousov, V.V. (2019). Which Antioxidant System Shapes Intracellular H₂O₂ Gradients? Antioxid. Redox Signal. *31*, 664–670.

Muik, M., Fahrner, M., Derler, I., Schindl, R., Bergsmann, J., Frischauf, I., Groschner, K., and Romanin, C. (2009). A Cytosolic Homomerization and a Modulatory Domain within STIM1 C Terminus Determine Coupling to ORAI1 Channels. J. Biol. Chem. *284*, 8421–8426.

Muik, M., Fahrner, M., Schindl, R., Stathopulos, P., Frischauf, I., Derler, I., Plenk, P., Lackner, B., Groschner, K., Ikura, M., and Romanin, C. (2011). STIM1 couples to ORAI1 via an intramolecular transition into an extended conformation. EMBO J. *30*, 1678–1689.

Nunes, P., and Demaurex, N. (2014). Redox regulation of store-operated Ca2+ entry. Antioxid. Redox Signal. *21*, 915–932.

Pak, V.V., Ezeriņa, D., Lyublinskaya, O.G., Pedre, B., Tyurin-Kuzmin, P.A., Mishina, N.M., Thauvin, M., Young, D., Wahni, K., Martínez Gache, S.A., et al. (2020). Ultrasensitive Genetically Encoded Indicator for Hydrogen Peroxide Identifies Roles for the Oxidant in Cell Migration and Mitochondrial Function. Cell Metab. *31*, 642–653.e6.

Parekh, A.B., and Putney, J.W., Jr. (2005). Store-operated calcium channels. Physiol. Rev. *85*, 757–810.

Park, C.Y., Hoover, P.J., Mullins, F.M., Bachhawat, P., Covington, E.D., Raunser, S., Walz, T., Garcia, K.C., Dolmetsch, R.E., and Lewis, R.S. (2009). STIM1 clusters and activates CRAC channels via direct binding of a cytosolic domain to Orai1. Cell *136*, 876–890.

Parrinello, M., and Rahman, A. (1981). Polymorphic transitions in single crystals: A new molecular dynamics method. J. Appl. Phys. *52*, 7182–7190.

Picard, C., McCarl, C.A., Papolos, A., Khalil, S., Lüthy, K., Hivroz, C., LeDeist, F., Rieux-Laucat, F., Rechavi, G., Rao, A., et al. (2009). STIM1 mutation associated with a syndrome of immunodeficiency and autoimmunity. N. Engl. J. Med. *360*, 1971–1980.

Piskounova, E., Agathocleous, M., Murphy, M.M., Hu, Z., Huddlestun, S.E., Zhao, Z., Leitch, A.M., Johnson, T.M., DeBerardinis, R.J., and Morrison, S.J. (2015). Oxidative stress inhibits distant metastasis by human melanoma cells. Nature *527*, 186–191.

Prakriya, M., and Lewis, R.S. (2015). Store-operated calcium channels. Physiol. Rev. *95*, 1383–1436.

Prevarskaya, N., Skryma, R., and Shuba, Y. (2011). Calcium in tumour metastasis: new roles for known actors. Nat. Rev. Cancer *11*, 609–618.

Prins, D., Groenendyk, J., Touret, N., and Michalak, M. (2011). Modulation of STIM1 and capacitative Ca2+ entry by the endoplasmic reticulum luminal oxidoreductase ERp57. EMBO Rep. *12*, 1182–1188.

Rhee, S.G. (1999). Redox signaling: hydrogen peroxide as intracellular messenger. Exp. Mol. Med. *31*, 53–59.

Saul, S., Gibhardt, C.S., Schmidt, B., Lis, A., Pasieka, B., Conrad, D., Jung, P., Gaupp, R., Wonnenberg, B., Diler, E., et al. (2016). A calcium-redox feedback loop controls human monocyte immune responses: The role of ORAI Ca2+ channels. Sci. Signal. *9*, ra26.

Schindelin, J., Arganda-Carreras, I., Frise, E., Kaynig, V., Longair, M., Pietzsch, T., Preibisch, S., Rueden, C., Saalfeld, S., Schmid, B., et al. (2012). Fiji: an open-source platform for biological-image analysis. Nat. Methods *9*, 676–682.

Schmidt, B., Alansary, D., Bogeski, I., Niemeyer, B.A., and Rieger, H. (2019). Reaction-diffusion model for STIM-ORAI interaction: The role of ROS and mutations. J. Theor. Biol. *470*, 64–75.

Shaw, P.J., Weidinger, C., Vaeth, M., Luethy, K., Kaech, S.M., and Feske, S. (2014). CD4^{+} and CD8^{+} T cell-dependent antiviral immunity requires STIM1 and STIM2. J. Clin. Invest. *124*, 4549–4563.

Sies, H., Berndt, C., and Jones, D.P. (2017). Oxidative Stress. Annu. Rev. Biochem. *86*, 715–748.

Soboloff, J., Rothberg, B.S., Madesh, M., and Gill, D.L. (2012). STIM proteins: dynamic calcium signal transducers. Nat. Rev. Mol. Cell Biol. *13*, 549–565.

Son, G.Y., Subedi, K.P., Ong, H.L., Noyer, L., Saadi, H., Zheng, C., Bhardwaj, R., Feske, S., and Ambudkar, I.S. (2020). STIM2 targets Orai1/STIM1 to the AKAP79 signaling complex and confers coupling of Ca^{2+} entry with NFAT1 activation. Proc. Natl. Acad. Sci. USA *117*, 16638–16648.

Sousa da Silva, A.W., and Vranken, W.F. (2012). ACPYPE—AnteChamber PYthon Parser interfacE. BMC Res. Notes *5*, 367.

Stanisz, H., Stark, A., Kilch, T., Schwarz, E.C., Müller, C.S., Peinelt, C., Hoth, M., Niemeyer, B.A., Vogt, T., and Bogeski, I. (2012). ORAI1 Ca(2+) channels control endothelin-1-induced mitogenesis and melanogenesis in primary human melanocytes. J. Invest. Dermatol. *132*, 1443–1451.

Stanisz, H., Saul, S., Müller, C.S., Kappl, R., Niemeyer, B.A., Vogt, T., Hoth, M., Roesch, A., and Bogeski, I. (2014). Inverse regulation of melanoma growth and migration by Orai1/STIM2-dependent calcium entry. Pigment Cell Melanoma Res. *27*, 442–453.

Stanisz, H., Vultur, A., Herlyn, M., Roesch, A., and Bogeski, I. (2016). The role of Orai-STIM calcium channels in melanocytes and melanoma. J. Physiol. *594*, 2825–2835.

Stathopulos, P.B., Zheng, L., Li, G.Y., Plevin, M.J., and Ikura, M. (2008). Structural and mechanistic insights into STIM1-mediated initiation of store-operated calcium entry. Cell *135*, 110–122.

Stathopulos, P.B., Schindl, R., Fahrner, M., Zheng, L., Gasmi-Seabrook, G.M., Muik, M., Romanin, C., and Ikura, M. (2013). STIM1/Orai1 coiled-coil interplay in the regulation of store-operated calcium entry. Nat. Commun. *4*, 2963.

Subedi, K.P., Ong, H.L., Son, G.Y., Liu, X., and Ambudkar, I.S. (2018). STIM2 Induces Activated Conformation of STIM1 to Control Orai1 Function in ER-PM Junctions. Cell Rep. *23*, 522–534.

Sun, S., Zhang, H., Liu, J., Popugaeva, E., Xu, N.J., Feske, S., White, C.L., 3rd, and Bezprozvanny, I. (2014). Reduced synaptic STIM2 expression and impaired store-operated calcium entry cause destabilization of mature spines in mutant presenilin mice. Neuron *82*, 79–93.

Trebak, M., Ginnan, R., Singer, H.A., and Jourd'heuil, D. (2010). Interplay between calcium and reactive oxygen/nitrogen species: an essential paradigm for vascular smooth muscle signaling. Antioxid. Redox Signal. *12*, 657–674.

Wang, J., Wolf, R.M., Caldwell, J.W., Kollman, P.A., and Case, D.A. (2004). Development and testing of a general amber force field. J. Comput. Chem. *25*, 1157–1174.

Wang, X., Wang, Y., Zhou, Y., Hendron, E., Mancarella, S., Andrake, M.D., Rothberg, B.S., Soboloff, J., and Gill, D.L. (2014). Distinct Orai-coupling domains in STIM1 and STIM2 define the Orai-activating site. Nat. Commun. *5*, 3183.

Waterhouse, A., Bertoni, M., Bienert, S., Studer, G., Tauriello, G., Gumienny, R., Heer, F.T., de Beer, T.A.P., Rempfer, C., Bordoli, L., et al. (2018). SWISS-MODEL: homology modelling of protein structures and complexes. Nucleic Acids Res. *46* (*W1*), W296–W303.

Winterbourn, C.C., and Hampton, M.B. (2008). Thiol chemistry and specificity in redox signaling. Free Radic. Biol. Med. *45*, 549–561.

Xiao, H., Jedrychowski, M.P., Schweppe, D.K., Huttlin, E.L., Yu, Q., Heppner, D.E., Li, J., Long, J., Mills, E.L., Szpyt, J., et al. (2020). A Quantitative Tissue-Specific Landscape of Protein Redox Regulation during Aging. Cell *180*, 968–983.e24.

Xie, K., Bunse, C., Marcus, K., and Leichert, L.I. (2019). Quantifying changes in the bacterial thiol redox proteome during host-pathogen interaction. Redox Biol. *21*, 101087.

Yoshikawa, S., Oh-Hora, M., Hashimoto, R., Nagao, T., Peters, L., Egawa, M., Ohta, T., Miyake, K., Adachi, T., Kawano, Y., et al. (2019). Pivotal role of STIM2, but not STIM1, in IL-4 production by IL-3-stimulated murine basophils. Sci. Signal. *12*, eaav2060.

Yuan, J.P., Zeng, W., Dorwart, M.R., Choi, Y.J., Worley, P.F., and Muallem, S. (2009). SOAR and the polybasic STIM1 domains gate and regulate Orai channels. Nat. Cell Biol. *11*, 337–343.

Zal, T., and Gascoigne, N.R.J. (2004). Photobleaching-corrected FRET efficiency imaging of live cells. Biophys. J. *86*, 3923–3939.

Zheng, L., Stathopulos, P.B., Schindl, R., Li, G.Y., Romanin, C., and Ikura, M. (2011). Auto-inhibitory role of the EF-SAM domain of STIM proteins in store-operated calcium entry. Proc. Natl. Acad. Sci. USA *108*, 1337–1342.

Zhu, J., Lu, X., Feng, Q., and Stathopulos, P.B. (2018). A charge-sensing region in the stromal interaction molecule 1 luminal domain confers stabilization-mediated inhibition of SOCE in response to *S*-nitrosylation. J. Biol. Chem. *293*, 8900–8911.

STAR★METHODS

KEY RESOURCES TABLE

REAGENT or RESOURCE	SOURCE	IDENTIFIER
Antibodies		
Anti-Orai1	Sigma-Aldrich	Cat#O8264; RRID: AB_1078883
Anti-GAPDH	Cell Signaling Technology	Cat#2118L; RRID: AB_561053
Anti-Mouse; HRP Conjugated	GE Healthcare	Cat#NA931; RRID: AB_772210
Anti-Rabbit; HRP Conjugated	GE Healthcare	Cat#NA9340; RRID: AB_772191
Biological Samples		
Human donor blood samples	UMG Göttingen blood bank (UMG, Ethics approval 2/3/18)	N/A
Chemicals, Peptides, and Recombinant Proteins		
Dulbecco's modified Eagle's (DMEM) medium	Thermo Fisher Scientific	Cat#41966029
MCDB153 basal medium	Biochrom	Cat#F8105
Leibovitz's L-15 medium	Biochrom	Cat#F21315
AIMV medium	Thermo Fisher Scientific	Cat#12055091
RPMI medium	Sigma Aldrich	Cat#R7388
OptiMEM medium	Thermo Fisher Scientific	Cat#51985034
DPBS	Thermo Fisher Scientific	Cat#14190250
Lipofectamine2000	Thermo Fisher Scientific	Cat#11668027
Fugene® HD	Promega GmbH	Cat#E2311
TransFectin	Bio-Rad	Cat#1703351
SF Cell Line 4D-NucleofectorTM X Kit L	Amaxa Nucleofector, Lonza	Cat#V4XC-2024
P3 Primary Cell 4D-NucleofectorTM X Kit L	Amaxa Nucleofector, Lonza	Cat#V4XP-3024
ImmunoCultTM Human CD3/CD28 T cell Activator	Stem Cell Technologies	Cat#10991
MTSEA-biotin	Biotinum	Cat#B-90066-1
Pierce Avidin-Agarose	Thermo Fisher Scientific	Cat#20219
Pierce ECL Western Blotting Substrate	Thermo Fisher Scientific	Cat#32106
Fura-2 AM	Thermo Fisher Scientific	Cat#F1221
Thapsigargin	Sigma-Aldrich	Cat#T9033
Fluoromount-G	Thermo Fisher Scientific	Cat#00495802
Critical Commercial Assays		
Dynabeads Untouched Human CD4 T Cells Kit	Invitrogen, Thermo Fisher Scientific	Cat#10449053
Cleavable ICAT Method Development kit	AB SCIEX	Cat#4337336
Cleavable ICAT Method Bulk kit	AB SCIEX	Cat#4337337
Deposited Data		
OxiMouse	(Xiao et al., 2020)	https://oximouse.hms.harvard.edu/download.html
STIM2 homology model	Protein Databank	PDB: 2MAJ and PDB: 4O9B
Redox proteomics	This publication	Table S1
Experimental Models: Cell Lines		
HEK293	ATCC	Cat#CRL-1573
HEK HA-Orai1 WT	(Kilch et al., 2013)	N/A
HEK Flp-In STIM2	This publication	N/A
Flp-In T-REx 293	Thermo Fisher Scientific	Cat#R78007
HEK Flp-In O1-TCM	This publication	N/A
HEK293 STIM1/STIM2 double knockout	(Emrich et al., 2019)	N/A

(Continued on next page)

Continued

REAGENT or RESOURCE	SOURCE	IDENTIFIER
WM3734	Meenhard Herlyn laboratory (The Wistar Institute, Philadelphia, USA)	N/A
1205Lu	Meenhard Herlyn laboratory (The Wistar Institute, Philadelphia, USA)	N/A
Oligonucleotides		
STIM2 siRNA sense 5′ UAA GCA GCA UCC CAC AUG ATT - dTdT 3′	Microsynth	N/A
STIM2 siRNA antisense 3′ dT dT - AUU CGU CGU AGG GUG UAC UAA 5′	Microsynth	N/A
Ctrl siRNA sense 5′ UUC UCC GAA CGU GUC ACG U - dTdT 3′	Microsynth	N/A
Ctrl siRNA antisense 3′ dTdT - AAG AGG CUU GCA CAG UGC A 5′	Microsynth	N/A
Recombinant DNA		
pCAGGS-O1-TCM	(Bogeski et al., 2010)	N/A
pcDNA5/FRT/TO	Thermo Fisher Scientific	Cat#V103320
poG44	Thermo Fisher Scientific	Cat#V600520
pcDNA5/FRT/TO-ORAI1-TCM	This publication	N/A
pEX-CMV-SPS1-YFP-STIM2	Addgene	Addgene Cat#18862
pEX-CMV-SPS1-YFP-STIM2 (cysteine to valine mutants)	This publication	N/A
spS1-HA-hSTIM2-EGFP or mCherry (cysteine to alanine mutants)	This publication	N/A
YFP-OASF2-CFP (cysteine to valine mutants)	This publication	N/A
HA-hSTIM2-ΔK17-EGFP or mCherry (cysteine to alanine mutants)	This publication	N/A
mCherry-hORAI1-TCM	This publication	N/A
pCMV-pL4-HyPer-DAAO-NES	(Pak et al., 2020)	N/A
Software and Algorithms		
FIJI / ImageJ	(Schindelin et al., 2012)	https://imagej.net/Welcome
Zeiss Zen (2.6)	Carl Zeiss Microscopy GmbH	N/A
TILLVision (4.0.1)	T.I.L.L. Photonics GmbH / FEI GmbH	N/A
Leica Application Suite LAS X (3.5.5)	Leica Microsystems	N/A
VisiView (2.1.1) and (4.2.0.0)	Visitron Systems GmbH	N/A
Biorad Quantity One (4.6.9)	Biorad	https://www.bio-rad.com/de-de/product/quantity-one-1-d-analysis-software?ID=1de9eb3a-1eb5-4edb-82d2-68b91bf360fb
Image Lab (3.0.1)	Biorad	https://www.bio-rad.com/de-de/product/image-lab-software?ID=KRE6P5E8Z
MaxQuant software (1.5.3.17, DE)	(Cox and Mann, 2008)	https://www.maxquant.org/
MATLAB (7.0.4)	The MathWorks, Inc.	https://de.mathworks.com/products/matlab.html
Python (3.7.7)	Python Software Foundation	http://www.python.org
Pandas (0.25.3)	https://conference.scipy.org/proceedings/scipy2010/mckinney.html	https://pandas.pydata.org/
PyMOL (1.8.5.0)	Schrödinger	https://pymol.org/2/#opensource
RStudio (1.1.456)	RStudio	https://rstudio.com/products/rstudio/download/#download

Continued

REAGENT or RESOURCE	SOURCE	IDENTIFIER
SWISS-MODEL (2019)	(Benkert et al., 2011; Waterhouse et al., 2018)	https://swissmodel.expasy.org/
GROMACS (2019)	(Abraham et al., 2015)	http://manual.gromacs.org/documentation/
AMBER14 (including antechamber)	https://ambermd.org/doc12/Amber14.pdf	https://ambermd.org/
ACPYPE (0.1.0)	(Sousa da Silva and Vranken, 2012)	http://ambermd.org/AmberTools.php
Gaussian 09	Gaussian Inc.	https://gaussian.com/glossary/g09/
Adobe Photoshop (CS6)	Adobe	https://www.chip.de/downloads/Photoshop-CS6_15182066.html

RESOURCE AVAILABILITY

Lead Contact

Further information and requests for resources and reagents should be directed to and will be fulfilled by the Lead Contact, Prof. Dr. med. Ivan Bogeski (ivan.bogeski@med.uni-goettingen.de).

Materials Availability

All unique/stable reagents generated in this study are available from the Lead Contact with a completed Materials Transfer Agreement.

Data and Code Availability

The redox proteomics data generated during this study are available in Table S1 and are available from the Lead Contact on request.

EXPERIMENTAL MODEL AND SUBJECT DETAILS

Cell lines

HEK293 (#CRL-1573, ATCC, Manassas, USA), HEK HA-Orai1 WT (Kilch et al., 2013), HEK Flp-In T-REx 293 (#R78007, Thermo Fisher Scientific GmbH, Schwerte, Germany), HEK293 STIM1/STIM2 double knockout (Emrich et al., 2019), HEK Flp-In STIM2 (this publication), HEK Flp-In O1-TCM (this publication), were cultivated in DMEM medium (#41966029, Thermo Fisher Scientific GmbH, Schwerte, Germany) supplemented with 10% FCS, 1% Penicillin/Streptomycin and antibiotics for selection (see Table S2). WM3734 and 1205Lu melanoma cells were a gift from Meenhard Herlyn (The Wistar Institute, Philadelphia, USA) and were cultivated in tumor medium (80% MCDB153 basal medium (#F8105, Biochrom, Berlin, Germany), and 20% Leibovitz's L-15 medium (#F21315, Biochrom, Berlin, Germany) supplemented with 1.68 mM $CaCl_2$ and 2% FCS). All cells were negative for mycoplasma and were maintained at 37°C in 5% CO_2.

Primary cell cultures

Primary human effector CD4$^+$ T cells were isolated as described in Bogeski et al. (2010) by a negative selection using Invitrogen Dynabeads Untouched Human CD4 T Cells Kit (#10449053, Thermo Fisher Scientific GmbH, Schwerte, Germany) from PBMCs obtained from leukoreduction system (LRS) chambers provided by the Blood bank (UMG, Ethics approval 2/3/18) by density gradient centrifugation and cultivated in AIMV (#12055091, Thermo Fisher Scientific GmbH, Schwerte, Germany) supplemented with 10% FCS. Naïve T cells were activated using the ImmunoCult™ Human CD3/CD28 T cell Activator (#10991, Stem Cell Technologies, Vancouver, Canada) 72 hours prior to nucleofection (see siRNA-mediated protein knockdown) and cultivated in RPMI medium (#R7388, Sigma-Aldrich, Munich, Germany) supplemented with 10% FCS.

METHOD DETAILS

Cell line transfection and reagents

HEK cell lines were transfected with 200 ng each plasmid (imaging) or with 2 μg each plasmid in 10 cm dishes along with, 3 μL Lipofectamine2000 (#11668027, Thermo Fisher Scientific GmbH, Schwerte, Germany) or Fugene® HD (#E2311, Promega GmbH, Mannheim, Germany) and 100 μL OptiMEM (#51985034, Thermo Fisher Scientific GmbH, Schwerte, Germany) according to manufacturer's instructions. Imaging was performed 24 – 48 hours after transfection, unless otherwise specified. Stable HEK Flp-In O1-TCM (HEKO1$_{TCM}$) cells were induced with 1 μg/mL doxycycline 6 - 12 hours before imaging.

All chemicals were purchased from Sigma-Aldrich (Munich, Germany), unless otherwise indicated. Plasmids used see Table S3 and the Key Resources Table.

siRNA-mediated protein knockdown

Transient knockdown was generated using siRNA from Microsynth (Balgach, Switzerland) (siSTIM2 sense: 5′ UAA GCA GCA UCC CAC AUG AUU - dTdT 3′, antisense: 3′ dT dT - AUU CGU CGU AGG GUG UAC UAA 5′; siCtrl sense: 5′ UUC UCC GAA CGU GUC ACG U - dTdT 3′, antisense: 3′ dTdT - AAG AGG CUU GCA CAG UGC A 5′). 1-3 million cells were transfected by nucleofection (Amaxa Nucleofector, Lonza GmbH, Cologne, Germany) using the SF Cell Line Kit for melanoma cell lines and P3 Primary Cell Kit for T cells (#V4XC-2024 and #V4XP-3024) according to manufacturer's instructions with 4 μL of a 20 μM siRNA stock solution. All measurements were performed 48 hours after transfection and the knockdown efficiency was confirmed as shown in Stanisz et al. (2012, 2014).

Redox proteomics

The OxICAT method was used according to the protocol of Leichert et al. (2008) using the reagents provided by AB SCIEX (Framingham, USA). Cleavable ICAT Method Development kit (#4337336) and Bulk kit (#4337337). Briefly, HEKS2$_{WT}$ (stable) cells were grown and treated with either 1 mM H$_2$O$_2$ (oxidized sample) or 2 mM DTT (reduced sample) for 30 min at room temperature. All used buffers were degassed and kept under hypoxic conditions over night. Cells corresponding to 100 μg of protein were lysed by sonication in denaturing alkylation buffer (DAB: 6 M Urea, 10 mM EDTA (ethylenediaminetetraacetic acid), 20 mM Tris-HCl (2-Amino-2-(hydroxymethyl)-1,3-propanediol hydrochloride) pH 8.5, 0.5% (w/v) SDS (sodium dodecyl sulfate)), including 20% (v/v) acetonitrile in presence of light-labeled (^{12}C) ICAT (isotope-coded affinity tag). Samples were precipitated and washed with 80% (v/v) acetone as described. Proteins were fully reduced with 1 mM TCEP (tris(2-carboxyethyl)phosphine hydrochloride) for 10 min at 37°C and labeled with heavy-labeled (^{13}C) ICAT following the same precipitation and washing steps. Samples were denatured using denaturing buffer (50 mM Tris-HCl, 0.1% SDS (w/v)) and digested with trypsin (0.125 μg/μL). Tryptic peptides were purified using cation exchange and avidin affinity chromatography according to the manufacturer's instructions. Cleavage of the biotin-tag was performed and resulting peptides were concentrated to dryness and dissolved in 0.1% (v/v) trifluoroacetic acid for LC-MS/MS analysis. Measurements were performed with a LTQ Orbitrap Elite instrument (Thermo Fisher Scientific GmbH, Schwerte, Germany) as described (Lindemann et al., 2013). Data analysis and quantification of cysteine oxidation was performed using the MaxQuant software (version 1.5.3.17, DE) (Cox and Mann, 2008) using the Homo_sapiens.GRCh38.pep.all (downloaded 12.2015 on http://uswest.ensembl.org/info/data/ftp/index.html) for the search engine Andromeda as described in Xie et al. (2019).

MTSEA-biotin assay

HEK293 cells were transfected using nucleofection (Amaxa Nucleofector, Lonza GmbH, Cologne, Germany) according to manufacturer's instructions. The cells were used 48 hours after transfection and incubated for 15 min at room temperature in Ringer's buffer containing 0.5 mM CaCl$_2$ (= untreated) and 1 mM H$_2$O$_2$ (= oxidized sample) or 1 mM H$_2$O$_2$ and additional 15 min with 2 mM DTT (= reduced sample). Cells were washed with PBSB (DPBS (Dulbecco's phosphate-buffered saline), pH adjusted to pH 8.0, with 1 mM MgCl$_2$ and 0.5 mM CaCl$_2$), permeabilized with PBSB + 0.001% (w/v) digitonin for 5 min and washed 3 times with PBSB. MTSEA-biotin labeling (0.5 mg/mL, 2-aminoethyl methanethiosulfonate hydrobromide; #B-90066-1, Biotinum, Fremont, USA) was performed for 40 min at room temperature. Cells were washed with PBSB + 0.1% (w/v) BSA (bovine serum albumin) and PBSB. Cells were detached with PBSB + 2 mM EDTA and collected by centrifugation (5 min, 4°C, 1000 g). The cell pellet was washed with PBSB and cells were lysed (PBS pH 7.4, 1% (v/v) Triton, 1 mM EDTA, proteinase inhibitors) using a cannula with 0.3 mm diameter. The lysate was incubated for 15 min at 4°C. Cell debris were removed by centrifugation for 20 min 4°C and 13,000 g. MTSEA-biotin labeled proteins were isolated from 500 μg cell lysate using avidin-coated beads (#20219, Thermo Fisher Scientific GmbH, Schwerte, Germany). Unspecific binders were removed by washing with lysis buffer + 250 mM NaCl. MTSEA-biotin labeled proteins were eluted using Laemmli buffer (4% (w/v) SDS, 125 mM Tris-HCl pH 6.8, 0.004% (w/v) bromophenol blue, 20% (v/v) glycerol, 10% (w/v) β-mercaptoethanol) for 15 min at 65°C. The samples were further processed by SDS-PAGE and immunoblotting.

Immunoblotting

25 μg of extracted protein were separated using 7% SDS–polyacrylamide gel electrophoresis (SDS-PAGE) and transferred onto nitrocellulose membranes. Primary antibody incubations were performed at 4°C overnight, blots were washed three times with PBS-T (PBS + 0.1% (v/v) Tween 20). Secondary antibodies were used 1:10,000 (anti-mouse, #NA931, GE Healthcare and anti-rabbit, #NA9340, GE Healthcare, Chicago, USA) and were applied for 1 hour at room temperature. Bands were detected with Pierce ECL Western Blotting Substrate (#32106, Thermo Fisher Scientific GmbH, Schwerte, Germany), after three washing steps with PBS-T. Different exposure times were used depending on the primary antibody using Biorad Quantity One (4.6.9) and Biorad Image Lab (3.0.1) for image acquisition and analysis. Primary antibodies used 1:1000: Orai1 (#O8264, Sigma-Aldrich, Munich, Germany), STIM2 (#S8572, Sigma-Aldrich, Munich, Germany) and GAPDH (glyceraldehyde 3-phosphate dehydrogenase; #2118L, Cell Signaling Technology, Danvers, USA).

"Oximouse" bioinformatics

The site stoichiometry data for all proteins from the OxiMouse project (data downloaded on the 20.05.2020 from https://oximouse. hms.harvard.edu/download.html) (Xiao et al., 2020) were prepared with Python 3.7.7 and Pandas 0.25.3 to skip all irrelevant columns, replace all NaN with 0 and extract the STIM2 specific data to Excel.

Fura-2-based Ca²⁺ imaging

Cells (150,000 - 300,000) were seeded on 25 mm round (No 1.5, #6310172, VWR, Radnor, USA) glass coverslips 24 - 48 hours before transfection. Fura-2-based measurements of cytosolic Ca^{2+} were performed as in Saul et al. (2016). Briefly, cells were loaded with 1 μM Fura-2 AM (#F1221, Thermo Fisher Scientific GmbH, Schwerte, Germany) in growth medium for 30 min at room temperature. The measurements were performed in Ringer's buffer (pH 7.4) containing 145 mM NaCl, 4 mM KCl, 10 mM Glucose, 10 mM HEPES (4-(2-hydroxyethyl)-1-piperazineethanesulfonic acid), 2 mM $MgCl_2$ and concentrations of $CaCl_2$ as indicated, or 0 mM $CaCl_2$ with 1 mM EGTA at room temperature and store depletion was facilitated using 1 μM Tg (thapsigargin, #T9033, Sigma-Aldrich, Munich, Germany). Ratiometric time-lapse imaging was performed on an Olympus microscope and analyzed with TILLVision 4.0.1 software (FEI GmbH, Munich, Germany) or using a Zeiss Axiovert S100TV equipped with a pE-340$_{fura}$ (CoolLED, Andover, United Kingdom) LED light source with LED 340 nm (excitation filter: 340/20) and 380 nm (excitation filter: 380/20) together with a T400 LP dichroic mirror and 515/80 emission filter, a sCMOS pco.edge camera and a Fluar 20x/0.75 objective. Data were analyzed with VisiView 4.2.0.0 software (Visitron Systems GmbH, Puchheim, Germany). The obtained 340 nm / 380 nm fluorescence ratios were converted to calibrated data using the equation $[Ca^{2+}] = K*(R - R_{min})/(R_{max} - R)$, while the values of K, R_{min}, and R_{max} were determined as described in Grynkiewicz et al. (1985).

Hydrogen peroxide measurements

Hydrogen peroxide was measured using the ratiometric protein sensor HyPer in Ringer's buffer containing 0.5 mM Ca^{2+}. HyPer-DAAO plasmids were transfected using Lipofectamine2000 or Fugene® HD as described above using 1 μg plasmid. Experiments were performed with a Zeiss Observer D1 equipped with a 20x Plan Apochromat (N.A. 0.8) objective, Axiocam 702 mono and LED system (Colibri, Zeiss) at 37°C. Images were acquired upon excitation at 420 nm (excitation filter: 420/40) and 505 nm (excitation filter: 500/15) together with a 515 nm dichroic mirror and 539/25 emission filter. Data were analyzed using Zen 2.6 software (Carl Zeiss Microscopy GmbH, Oberkochen, Germany).

Electrophysiological recordings

Electrophysiological experiments were performed 24 to 34 hours after transiently transfecting HEK293 cells with TransFectin (#1703351, Bio-Rad Laboratories, Hercules, USA) using 1 μg of Orai1-CFP and 1 μg STIM2 constructs. Patch-clamp recordings in whole-cell configuration were performed at 21–25°C. An Ag/AgCl electrode was used as reference electrode. Voltage ramps were applied every 5 s from a holding potential of 0 mV, covering a range of −90 to +90 mV over 1 s. Experiments were run with 10 mM Ca^{2+} bath solution, while store-dependent activation was induced by buffering cytosolic Ca^{2+} with 20 mM EGTA. For passive store depletion, the internal pipette solution included: 145 mM Cs methane sulphonate, 20 mM EGTA, 10 mM HEPES, 8 mM NaCl and 3.5 mM $MgCl_2$; pH 7.2. Standard extracellular solution consisted of: 145 mM NaCl, 10 mM HEPES, 10 mM $CaCl_2$, 10 mM Glucose, 5 mM CsCl and 1 mM $MgCl_2$; pH 7.4. A liquid junction potential correction of +12 mV was applied, resulting from a Cl^{-}-based bath solution and a sulphonate-based pipette solution. All currents were leak corrected by subtracting the initial voltage ramps obtained shortly after break-in with no visible current activation from the measured currents or at the end of the experiment using La^{3+} (10 μM).

OASF2 FRET microscopy

Confocal FRET microscopy was performed on HEK293 cells transiently transfected with TransFectin using 1 μg plasmid. The transfected cells were grown on coverslips for 24 hours and subsequently transferred to an extracellular solution consisting of 140 mM NaCl, 5 mM KCl, 1 mM $MgCl_2$, 2 mM $CaCl_2$, 10 mM glucose and 10 mM HEPES buffer (adjusted to pH 7.4 with NaOH). A QLC100 Real-Time Confocal System (VisiTech Int.) connected to two Photometrics CoolSNAPHQ monochrome cameras (Roper Scientific) and a dual-port adaptor (dichroic: 505lp; cyan emission filter: 485/30; yellow emission filter: 535/50; Chroma Technology Corp.) was used to record fluorescence images. This system was attached to an Axiovert 200M microscope (Zeiss, Germany) in conjunction with two diode lasers (445 nm, 515 nm) (Visitron Systems). Visiview 2.1.1 software (Visitron Systems) was used for image acquisition and control of the confocal system. Illumination times for CFP/FRET and YFP images that were recorded consecutively with a minimum delay were about 600 ms. Image correction to address cross-talk and cross-excitation was performed prior to the calculation. To this end, appropriate cross-talk calibration factors were determined for each construct on each day of the FRET experiment. After threshold determination and background subtraction, the corrected FRET (E_{app}) was calculated on a pixel-to-pixel basis with a custom-made software integrated into MATLAB 7.0.4 according to the method published by Zal and Gascoigne (2004), with a microscope specific constant G value of 2.0.

STIM2 cluster analysis and STIM2-STIM2 FRET

HEKO1$_{WT}$ cells were transfected either with HA-hSTIM2ΔK17-EGFP + HA-hSTIM2ΔK17-mCherry or HA-hSTIM2-C313A-ΔK17-EGFP + HA-hSTIM2-C313A-ΔK17-mCherry as described above and seeded on 12 mm round (No 1.5, #6302190, VWR, Radnor,

USA) poly-D-lysine (50 µg/mL) coated coverslips 24 hours before usage. Cells were washed once with Ca^{2+} free DPBS (#14190250, Thermo Fisher Scientific GmbH, Schwerte, Germany) and treated for 15 min with 1 µM Tg (thapsigargin, #T9033, Sigma-Aldrich, Munich, Germany) or 100 µM H_2O_2 followed by 15 min 1 µM Tg (all in Ca^{2+} free DPBS). Cells were fixed with 4% (w/v) PFA (paraformaldehyde) in DPBS buffer for 15 min at room temperature and mounted with Fluoromount-G (#00495802, Thermo Fisher Scientific GmbH, Schwerte, Germany) on glass slides. Imaging was performed on a Zeiss LSM800 setup equipped with LCI Plan-Neofluar 63x (N.A. 1.3) glycerin immersion objective. Images were acquired with Zen 2.6 software (Zeiss, Oberkochen, Germany) using multi-alcali-PMT detectors splitting the signals at 590 nm for GFP (488 nm; SP545 filter), mCherry (561 nm; no filter) and FRET (488 nm, no filter) using an averaging of 4 and unidirectional fast image acquisition. Images were analyzed using a customized ImageJ macro. Briefly, following background subtraction, cells borders were marked and their area was recorded. Cluster area was measured with the ImageJ Particle Analyzer in binarized images resulting from intensity-based thresholding in all three channels. FRET was calculated using the bleed-through (obtained by samples expressing either the GFP or mCherry tagged STIM2) and background corrected FRET/donor ratio.

$$FRET/donor\ ratio = \frac{(FRET - background) - [(donor - background) \cdot CFd] - [(acceptor - background) \cdot CFa]}{(donor - background)} \quad \text{Equation 1}$$

*CF: correction factor for donor and acceptor bleed-through

STIM2-ORAI1$_{TCM}$ cluster analysis and STIM2-ORAI1$_{TCM}$ FRET

HEK293 cells were transfected either with HA-hSTIM2ΔK17-EGFP + mCherry-hORAI1-TCM or HA-hSTIM2-C313A-ΔK17-EGFP + mCherry-hORAI1-TCM and samples were prepared and analyzed as described above for STIM2-STIM2 cluster analysis.

FLIM microscopy

Time-correlated single photon counting (TCSPC) - based fluorescence lifetimes were recorded with a Leica SP8 FALCON laser scanning confocal microscope (Leica Microsystems, Mannheim, Germany). 1×10^5 donor-based photons/pixel were recorded within the donor-specific 500 – 525 nm emission window with a 63x (1.4 NA) objective upon pulsed (40 MHz) 488 nm excitation. The phasor analysis approach provided within the Leica Application Suite (3.5.5) was used to identify different molecular species populations based on their respective lifetime. FRET efficiencies were obtained by applying the FRET trajectory approach of the phasor analysis method. For details, see Digman et al. (2008). The samples, HEKO1$_{WT}$ cells expressing either with HA-hSTIM2ΔK17-EGFP + HA-hSTIM2ΔK17-mCherry or HA-hSTIM2-C313A-ΔK17-EGFP + HA-hSTIM2-C313A-ΔK17-mCherry, were treated and prepared as for STIM2 cluster analysis (see above). Samples with single GFP or untransfected HEKO1$_{WT}$ cells were used as controls to establish the FRET efficiency.

MD simulations
Model preparation

The STIM2 model was prepared based on the STIM1 CC1α3-CC2 homodimer NMR structure (Stathopulos et al., 2013) taken from the Protein Databank (PDB: 2MAJ) (Berman et al., 2000). The N-terminal part of each STIM1 monomer was extended by 10 residues in α-helical conformation according to the crystal structure of CC1 of STIM1 (PDB: 4O9B) (Cui et al., 2013). The final STIM1-dimer model contained two monomers each consisting of residues 302-387. A homology model for the STIM2 homodimer was generated using SWISS-MODEL (2019) (Benkert et al., 2011; Waterhouse et al., 2018). The sequence identity between the modeled regions of STIM1 and STIM2 was computed to 76.74% and the generated homology STIM2 dimer model obtained a QMEAN-score of −1.56 (Benkert et al., 2011). Each monomer of the final STIM2 CC1α3-CC2 homodimer contained residues 306-391 (Figure 5A).

Parameterization of C313 S-Sulfonylation

In order to investigate the effect of S-sulfonylation of C313 in STIM2, force field parameters for the modified amino acid were generated using Antechamber within the AMBER14 software package. Initial coordinates of S-sulfonylated cysteine were obtained from the PDB (PDB: 2H4E) (Gales et al., 2007). Following the protocol for parameterization of non-standard amino acids (http://ambermd.org/), the N- and C-termini of a single S-sulfonylated cysteine residue were capped with an acetyl- and N-methyl-group in α-helical conformation, respectively, using PyMOL (1.8.5.0).

Full geometry optimization with restraints on backbone dihedral angles was performed with the Hartree–Fock level of theory (Hehre, 1976) (HF/6-31G*) in Gaussian 09. Partial charges of the optimized structure were calculated and assigned to individual atoms using the Restrained Electrostatic Potential (RESP) method (Cornell et al., 1993). Complete AMBER14SB force field parameters (Maier et al., 2015) were generated with Antechamber, thereby, AMBER14SB protein atom types were used for all standard amino acid atoms while the sulfonic acid sulfur atom and associated bond parameters were described by the Generalized AMBER Force Field (GAFF) (Wang et al., 2004). Finally, the C313-S-sulfonylated STIM2 homodimer was modeled by manually inserting the modified amino acid using PyMOL. Protein AMBER14SB force field parameters were generated with AMBER14 and converted to input files for GROMACS 2019 (Abraham et al., 2015) using ACPYPE 0.1.0 (Sousa da Silva and Vranken, 2012).

Molecular dynamics simulations

STIM2 homodimers were solvated in dodecahedron simulation boxes (x, y ≈ 10.25 nm, z ≈ 7.25 nm) at a 0.15 M salt concentration. Simulation systems contained one STIM2 CC1α3-CC2 homodimer, roughly 24,000 water molecules and approx. 140 ions (sodium

and chloride). Both the C313 and C313-Sulf systems were first minimized (1,000 steps) with the steepest descent algorithm and subsequently equilibrated for 1 ns with position restraints on all heavy atoms, followed by a 10 ns long simulation with restraints on the backbone atoms only. The equilibrated system was used as a starting structure for four different C313 and C313-Sulf simulations, respectively. The simulations were initialized with different atom starting velocities and were conducted for 500 ns. The temperature was kept constant at 310 K with the v-rescale algorithm (Bussi et al., 2007) with a time constant of 0.1 ps. The pressure was coupled isotropically to 1 bar (τ_p = 2.0 ps) with the Berendsen barostat (Berendsen et al., 1984) for the equilibration simulations and Parrinello-Rahman (Parrinello and Rahman, 1981) for the production run simulations. Charged interactions were calculated with Particle Mesh Ewald (Darden et al., 1993) with a real space cut-off of 1.0 nm and the van der Waals potential was shifted to zero with r_{vdw} = 1.0 nm. All simulations were performed in GROMACS 2019.x (Abraham et al., 2015) with parameters of the AMBER14SB and Generalized AMBER force field (Maier et al., 2015; Wang et al., 2004).

Data analysis
The root mean square deviations (RMSDs) for STIM2 backbone atoms were calculated for each simulation after least-square fitting all backbone atoms of the model STIM2 CC1α3-CC2 dimer. The average root mean square fluctuations (RMSFs) for each residue were determined based on all four simulations and both STIM2 CC1α3-CC2 monomers. For this purpose, the final 200 ns of each simulation was divided into 10 ns intervals wherein the RMSF was calculated separately for each monomer after least-square fitting the backbone atoms. The mean RMSF and standard error was calculated based on all eight temporal RMSF averages. Similarly, the average helicity was assessed by determining the temporal amount over the final 200 ns of each simulation for which a residue was helical (α- or 3_{10}-helix).

Individual residue-residue interactions either within the CC1α3-CC2 monomers (*intra*) or between the two CC1α3-CC2 monomers (*inter*) were analyzed based on pairwise minimal distances of side chain residues during the final 200 ns.

The solvent accessibilities of the two individual ORAI binding sites were calculated for all 20 STIM1 CC1$_{[TM-distal]}$-CC2 NMR structures in its ORAI bound and free conformation (Stathopulos et al., 2013), respectively, and for the model STIM2 CC1$_{[TM-distal]}$-CC2 structures obtained in the final 200 ns of the simulations. The binding sites in STIM1 were defined based on the residues interacting with ORAI (Figure S5D) and equivalent residues were chosen for STIM2 (Figure 6F; Figure S5A, alignment).

Generation of HEKO1$_{TCM}$ cell line
pcDNA5/FRT/TO-ORAI1-TCM (TM: Triple Cysteine Mutant C126S; C143S; C195S) was constructed by amplifying ORAI1-TCM from pCAGGS-O1-TCM (Bogeski et al., 2010) using 5′-GCG CGC GGA TCC ATG CAT CCG GAG CCC GCC CCG CC-3′ forward and 5′-GCG CGC GCG GCC GCC TAG GCA TAG TGG CTG CCG GGC GTC-3′ reverse and cloned via *Not*I and *BamH*I into pcDNA5/FRT/TO (#V103320, Thermo Fisher Scientific GmbH, Schwerte, Germany). The vector was transfected as described above into HEK Flp-In T-REx 293 cells along with poG44 (#V600520, Thermo Fisher Scientific GmbH, Schwerte, Germany), cells were treated according to manufacturer's instructions and selected by clonal selection. O1$_{TCM}$ expression was induced 12 - 24 hours after transfection with 1 μg/mL doxycycline for 6 - 12 hours. Characterization of the cell line see Figures S1H–S1J.

Construction of plasmids
pEX-CMV-SPS1-YFP-STIM2 (#18862, Addgene; kindly provided by Tobias Meyer): The mentioned mutations P38L, V222I and E575V (depositors comment) were corrected and cysteine to valine point mutations were introduced in STIM2 plasmids (accession number NM_020860) using the QuikChange site-directed mutagenesis kit (Agilent Technologies, Santa Clara; USA).

YFP-OASF2-CFP: For creation of the double-tagged OASF2 construct, CFP was integrated into pEYFP-C2 (Clontech, Kusatsu, Japan) via *Sac*II and *Xba*I. Finally, the STIM2 fragment (OASF2 residues 237-478) was cloned into this modified vector via *EcoR*I and *Sac*II and mutations were introduced via QuikChange site-directed mutagenesis kit (Agilent Technologies, Santa Clara; USA).

spS1-HA-hSTIM2-EGFP and spS1-HA-hSTIM2-mCherry: Previously generated HA-hSTIM2 pEGFP-N1 plasmid containing no fluorescent protein tag was double-digested with *Nde*I and SalI-HF restriction enzymes. The 2.668 kB insert containing CMV promoter as well as signal sequence of STIM1 followed by HA-hSTIM2 until the stop codon was gel purified and ligated into *Nde*I and SalI-HF digested and purified pEGFP-N1 and pMCherry-N1 vectors. Site-directed mutagenesis of both resulting constructs by 5′-CTT TTT AAG AAG AAA TCT AAG TCG ACG GTA CCG CGG GCC C-3′ forward and 5′-GGG CCC GCG GTA CCG TCG ACT TAG ATT TCT CTT AAA AAG-3′ reverse primers led to the removal of the stop codon of hSTIM2 and brought the C-terminal EGFP or mCherry in frame. Cysteine to alanine mutations were introduced by site-directed mutagenesis using 5′-GCA AAG GAG GAG GCT GCT CGG CTG AGA GAG C-3′ forward or 5′-CTA AGG GAG GGA GCT GAA GCT GAA TTG AGT AGA CGT CAG-3′ forward primer to generate C302A or C313A mutant, respectively.

HA-hSTIM2-ΔK-EGFP and HA-hSTIM2-ΔK-mCherry plasmids: SpS1-HA-hSTIM2-EGFP and spS1-HA-hSTIM2-mCherry plasmids were double-digested with *EcoR*I-HF and SalI-HF restriction enzymes. The resulting vector backbones missing fragments encoding for hSTIM2 residues 94-746 were gel purified. YFP-hSTIM2-ΔK was mutagenized using 5′-CCT TTG TCA TAA TGG AGA GTC GAC AAA AGC AAA AAG CCA TCA AA-3′ forward and 5′-TTT GAT GGC TTT TTG CTT TTG TCG ACT CTC CAT TAT GAC AAA GG-3′ reverse primers to create a SalI restriction site after the codon of E729 residue. The mutagenized plasmid was digested with *EcoR*I-HF and SalI-HF restriction enzymes and an insert encoding for hSTIM2 residues 94-729 was purified. This insert was ligated into the above generated vectors. This resulted in HA-hSTIM2-ΔK-EGFP and HA-hSTIM2-ΔK-mCherry plasmids lacking last 15 residues (K-rich domain) of hSTIM2. Cysteine to alanine mutations were introduced by amplification of STIM2 fragments with pairs of primers

5′-GGA AGC TCT TCA AAC AAT ACA TAA ACA AAT GG-3′ forward and 5′-GTT CTG CAT ACT GAC GTC TAC TCA ATT CCG CTT CAG CTC CCT CCC TTA GCT CTC-3′ reverse or 5′-GAG AGC TAA GGG AGG GAG CTG AAG CGG AAT TGA GTA GAC GTC AGT ATG CAG AAC-3′ forward and 5′-GGG ACA CCT CAT CTC TTG ATA TCT TTC G-3′ reverse. Purified fragments were used for overlap extension PCR, using primers 5′-GGA AGC TCT TCA AAC AAT ACA TAA ACA AAT GG-3′ forward and 5′-GGG ACA CCT CAT CTC TTG ATA TCT TTC G-3′ reverse. PCR-product was purified and digested with *Eco*RI/*Xho*I (#R0101S, #R0146S, NEB) restriction enzymes. Digested PCR-product was cloned into HA-hSTIM2-ΔK17-EGFP and mCherry (digested with *Eco*RI/*Xho*I).

All the above-mentioned HA and EGFP or mCherry tagged plasmids contained a 13-residue long linker (STVPRARDPPVAT) between hSTIM2 and EGFP or mCherry. EGFP always contained monomeric A207K mutation.

mCherry-hORAI1-TCM plasmid: hOrai1-TCM cDNA encoding the residues 43 to 273 from hOrai1-C126S-C143S-C195S pCAGGS-IRES-GFP (Bogeski et al., 2010) was replaced in mCherry-hOrai1 peGFP-N1 (kindly provided by Dr. Matthias Seedorf, Heidelberg University, Germany) using *Apa*I / *Sac*I-HF enzymes from NEB.

The integrity of all resulting mutants was confirmed by sequence analysis (Eurofins Genomics, Luxembourg, Luxembourg or Microsynth Seqlab GmbH, Göttingen, Germany).

QUANTIFICATION AND STATISTICAL ANALYSIS

Data obtained from experiments were analyzed or processed using Zeiss Zen 2.6, TILLVision 4.0.1, Leica Application Suite LAS X 3.5.5, VisiView 2.1.1 and 4.2.0.0, Biorad Quantity One 4.6.9, Image Lab 3.0.1, MATLAB 7.0.4, MaxQuant software 1.5.3.17, Python 3.7.7, Pandas 0.25.3, ImageJ or FIJI and Microsoft Excel. MD simulation data were generated as described in Method Details and visualized using PyMOL 1.8.5.0, RStudio 1.1.456 and Adobe Photoshop CS6. Data are presented as mean mean ± SEM and indicated *n* values correspond to independent experiments or for imaging experiments and electrophysiological recordings to the number of cells. Statistical significance was tested with unpaired, two-tailed Student t test unless otherwise specified. The significant differences are indicated by asterisks $*p < 0.05$; $**p < 0.01$; $***p < 0.005$.